SUBMITTED: 13 JUNE 2000 ; REVISED: 3 MAY 2001
Preprint typeset using LaTeX style emulateapj

THE FIRST DETECTIONS OF THE EXTRAGALACTIC BACKGROUND LIGHT AT 3000, 5500, AND 8000Å (I): RESULTS

REBECCA A. BERNSTEIN[1,2,3]
WENDY L. FREEDMAN[2]
BARRY F. MADORE[2,4]
1) Division of Math, Physics, and Astronomy, California Institute of Technology, Pasadena, CA 91125
2) Carnegie Observatories, 813 Santa Barbara St, Pasadena, CA 91101
3) rab@ociw.edu, Hubble Fellow
4) NASA/IPAC Extragalactic Database, California Institute of Technology, Pasadena, CA 91125

Submitted: 13 June 2000 ; Revised: 3 May 2001

ABSTRACT

We present the first detection of the mean flux of the optical extragalactic background light (EBL) at 3000, 5500, and 8000Å. Diffuse foreground flux at these wavelengths comes from terrestrial airglow, dust–scattered sunlight (zodiacal light), and dust–scattered Galactic starlight (diffuse Galactic light). We have avoided the brightest of these, terrestrial airglow, by measuring the absolute surface brightness of the night sky from above the Earth's atmosphere using the Wide Field Planetary Camera2 (WFPC2) and Faint Object Spectrograph (FOS), both aboard the Hubble Space Telescope (HST). On the ground, we have used the duPont 2.5 m Telescope at Las Campanas Observatory (LCO) to obtain contemporaneous spectrophotometry of "blank" sky in the HST field of view to measure and then subtract foreground zodiacal light from the HST observations. We have minimized the diffuse Galactic light in advance by selecting the HST target field along a line of sight with low Galactic dust column density, and then estimated the low–level Galactic foreground using a simple scattering model and the observed correlation between thermal, 100μm emission and optical scattered flux from the same dust. In this paper, we describe the coordinated LCO/HST program and the HST observations and data reduction, and present the resulting measurements of the EBL.

Galaxies brighter than $V = 23$ AB mag are not well sampled in an image the size of the WFPC2 field of view. We have therefore measured the EBL from unresolved and resolved galaxies fainter than $V = 23$ AB mag by masking out brighter galaxies. We write as EBL23 to emphasize this bright magnitude cut–off. From absolute surface photometry using WFPC2 and ground–based spectroscopy, we find mean values for the EBL23 of 4.0 (±2.5), 2.7 (±1.4), and 2.2 (±1.0) in units of $\times 10^{-9}$ergs s^{-1} cm^{-2} sr^{-1} Å^{-1} in the F300W, F555W, and F814W bandpasses, respectively. The errors quoted are 1σ combined statistical and systematic uncertainties. The total flux measured in resolved galaxies with $V > 23$ AB mag by standard photometric methods is roughly 15% of the EBL23 flux in each band. We have also developed a new method of source photometry, uniquely suited to these data, with which we can measure the ensemble flux from detectable sources much more accurately than is possible with standard methods for faint galaxy photometry. Using this method, we have quantified systematic biases affecting standard galaxy photometry, which prevent light from being recovered in isophotes within a few percent of the sky level. These biases have a significant effect on faint galaxy counts. The flux from resolved sources as measured by our ensemble photometry method is 3.2 (± 0.22), 0.89 (± 0.01), and 0.76 (± 0.01) in units of $\times 10^{-9}$ ergs s^{-1} cm^{-2} sr^{-1} Å^{-1} in the F300W, F555W, and F814W bandpasses, respectively, with 1σ combined errors. These values, the total flux from resolved sources, represent *absolute minima* for the EBL23 in each band, and are roughly 30% of the mean flux we measure for the total EBL23.

Subject headings: Diffuse radiation — cosmology: observations — galaxies: photometry — techniques: photometric — interplanetary medium — ISM: dust

1. INTRODUCTION

The Extragalactic Background Light (EBL) is the integrated, mean surface brightness of both resolved and unresolved extragalactic sources. In wavelength range of these observations (2500–9500Å), the EBL is dominated by flux from stellar nucleosynthesis at redshifts $z \lesssim 9$, and also includes flux from gravitational potential energy such as accreting black holes (Fabian & Iwasawa 1999), brown dwarfs, gravitationally collapsing systems, and possibly decaying particles. As such, the EBL is the fossil record of the star formation history of the universe and a fundamental measure of the luminous energy content of the universe. As we show in Figure 1, upper limits from previous attempts to measure the EBL and lower limits from integrated galaxy counts constrain the EBL to an expected level of roughly 1×10^{-9} ergs s^{-1} cm^{-2} sr^{-1} Å^{-1} at 5500Å, or 28.2 AB mag arcsec^{-2}.[1] Because the combined flux from foreground airglow, zodiacal light, and diffuse galactic light (also plotted in Figure 1) is at least 100 times brighter than the EBL, a detection of the EBL requires measurement accuracies of better than 1%.

[1] All surface brightnesses are specified in ergs s^{-1} cm^{-2} sr^{-1} Å^{-1} unless specifically noted otherwise. AB mag is defined as AB mag$= -2.5 \log F_\nu - 48.6$, as usual, with F_ν given in ergs s^{-1} cm^{-2} Hz^{-1}.

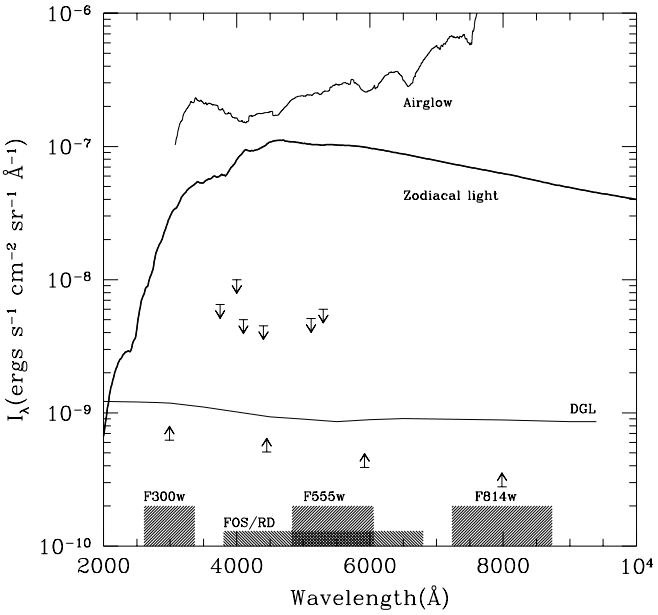

FIG. 1.— Relative surface brightnesses of foreground sources, upper limits on the EBL23 (see §1), and lower limits based on the integrated flux from resolved galaxies ($V_{555} > 23$ AB mag) in the HDF (Williams *et al.* 1996). The spectral shape and mean flux of zodiacal light and of diffuse galactic light (DGL) are shown at the levels we detect in this work. The airglow spectrum is taken from Broadfoot & Kendall (1968) and is scaled to the flux level we observe at 3800–5100Å (see §9). The effective bandpasses for our HST observations are indicated at the bottom of the plot.

Previous attempts to measure the optical EBL have employed a variety of different approaches. Mattila (1976) attempted to isolate the EBL by differencing integrations on and off the line of sight to "dark" clouds at high Galactic latitude, under the assumption that the clouds acted as a "blank screens," spatially isolating all foreground contributions from the background. This pioneering work produced upper limits and identified both the rapid temporal variability of terrestrial airglow and extinction and the spatial variability of diffuse Galactic light, which proved to be the primary obstacles to these early efforts to measure the EBL. Toller (1983) later attempted to avoid both atmospheric and zodiacal foregrounds by using data taken with the *Pioneer 10* spacecraft at a distance of 3 AU from the Sun, beyond the zodiacal dust cloud. Poor spatial resolution (2°), however, prevented the accurate subtraction of discrete Galactic stars, let alone the diffuse Galactic component from these data. Dube, Wilkes, & Wilkinson (1977, 1979) made the first effort to measure and subtract foreground contributions explicitly based on geometrical modeling of airglow and Galactic foregrounds but including spectroscopic measurement of the zodiacal light (ZL) flux by a technique similar to that which we have adopted. Rapid variability caused uncertainty in their airglow subtraction which dominated the errors in their results.

In this work, we take advantage of the significant gains in technology and in understanding of the foreground sources which have been achieved since the last attempts to measure the optical EBL (see Mattila 1990 for a review). The most significant technological advance is panoramic, linear CCD detectors. Those on-board HST allowed us to completely avoid bright, time–variable airglow and provide sub–arcsecond spatial resolution. High spatial resolution allowed us to resolve stars to $V \sim 27.5$ mag and thereby eliminate the possibility of significant contamination from unidentified Galactic stars in the field. Ground–based spectrophotometry with CCDs also made possible much more accurate measurement of the foreground zodiacal light than could be achieved with narrow–band filters and photometers, as were used by Dube, Wickes, & Wilkinson (1977, 1979). Finally, IRAS has provided maps of the thermal emission from dust at high Galactic latitudes. We have use the IRAS maps to select a line of sight for these observations which has a low column density of Galactic dust in order to minimize the DGL contribution caused by dust–scattered starlight, and also to estimate the low–level DGL which cannot be avoided.

Our measurement of the EBL utilizes three independent data sets. Two of these are from HST: (1) images from the Wide Field Planetary Camera 2 (WFPC2) using the F300W, F555W, and F814W filters, each roughly 1000Å wide with central wavelengths of 3000, 5500, and 8000Å, respectively; and (2) low–resolution spectra (300Å per resolution element) from the Faint Object Spectrograph (FOS) covering 3900–7000Å. The FOS data were taken in parallel observing mode with the WFPC2 observations. While flux calibration of WFPC2 images and FOS spectra achieve roughly the same accuracy for point source observations, the increase in spatial resolution, 10^4 times larger field of view, lower instrumental background, and absolute surface brightness calibration achievable with WFPC2 make it better suited than FOS to an absolute surface brightness measurement of the EBL. Nonetheless, the FOS observations do provide a second, independent measurement of the total background flux of the night sky, also free of terrestrial airglow and extinction, but with greater spectral resolution than the WFPC2 images. The third data set consists of long–slit spectrophotometry of a region of "blank" sky within the WFPC2 field of view. These data were obtained at the 2.5m duPont telescope at Las Campanas Observatory (LCO) using the Boller & Chivens spectrograph simultaneously with one visit of the HST observations (6 of 18 orbits).

The flow chart in Figure 2.1 summarizes the reduction procedures for each data set used in this measurement, the results obtained from each data set individually, and the coordination of those results to produce a measurement of the EBL. In this paper, we begin by describing the foreground sources in §2 and the details of HST scheduling in §3. The observations and data reduction of both HST data sets, WFPC2 and FOS, are discussed in detail in this paper. WFPC2 observations and data reduction are discussed in §4. In §5, we present the first results from the WFPC2 data, which are measurements of the total sky flux (foregrounds plus background) in each bandpass. The FOS observations, data reduction, and results are discussed in §6 and §7. The modeling of diffuse Galactic light is discussed in §8. The LCO data and measurement of ZL are discussed in Bernstein, Freedman & Madore (2001b, henceforth Paper II). A summary of that work is given in §9. In §10, we present a measurement of the minimum

flux of the EBL from resolved sources, which can be made using the WFPC2 data alone. The implications of that result are also discussed in §10. Finally, in §11 we combine the results of the individual data sets and modeling (horizontal connections shown in the flow chart) to obtain a measurement of the EBL. The implications of these results are discussed in Bernstein, Freedman & Madore (2001c, henceforth Paper III).

2. FOREGROUNDS

The contribution from foreground sources to the flux of the night sky is at least two orders of magnitude brighter than the expected extragalactic signal. That is, the combined flux from foreground sources is roughly 100×10^{-9} ergs s^{-1} cm^{-2} sr^{-1} Å^{-1} (or 23.2 AB mag arcsec^{-2}) (see Figure 1). A detection of the EBL therefore requires the measurement of both the total background and the individual foreground sources with an accuracy of roughly 1% of the total sky surface brightness, or $\sim 1\times10^{-9}$ ergs s^{-1} cm^{-2} sr^{-1} Å^{-1} at 5500Å (28.2 AB mag arcsec^{-2}). Each of the foreground sources, and our approach to minimizing and measuring them, are described briefly in the following sections.

2.1. *Terrestrial Airglow and Extinction*

Atmospheric emission is the brightest component of the night sky as seen from the Earth's surface. The mean flux and line strengths of the molecular, atomic, and continuum emission which produce "airglow" can vary by several percent on time-scales of minutes due to changes in atmospheric column densities throughout the night, stimulation by small meteorites, and photo-chemical excitation and de-excitation within several hours of twilight (see Chamberlain 1966 for background, Dube *et al.* 1979, and Paper II). The mean airglow flux can be predicted based on the line-of-sight path-length through the atmosphere, but the accuracy of this method is limited to a few percent. Airglow subtraction has dominated the errors in several previous attempts to measure the EBL (see Dube et al. 1979 and the discussion in Mattila 1990). However, the only significant airglow emission seen in the upper atmosphere from HST occurs at wavelengths shorter than 2000Å and only on the daytime side of the orbit (see Lyons et al. 1993 and reference therein). We have therefore entirely avoided optical airglow by using HST as the primary instrument in measuring the EBL.

2.2. *Zodiacal Light (ZL)*

Zodiacal light is sunlight scattered off of dust grains in the solar system, and it can be as bright as 1500×10^{-9}ergs s^{-1} cm^{-2} sr^{-1} Å^{-1} in the ecliptic plane. The ZL is faintest at viewing angles (heliocentric longitude) 130–170 degrees away from the Sun, where scattering angles are large, and at ecliptic latitudes greater than 30 degrees, where the interplanetary dust (IPD) column densities are lowest. To within 10%, the mean flux of the ZL is predictable as a function of scattering geometry and ecliptic latitude; however, this is not accurate enough for our purposes. Instead, we have measured the ZL flux directly using detailed a priori knowledge of its intrinsic spectrum. Observations of the ZL (Leinert *et al.* 1981, Murthy *et al.* 1990, Matsuura *et al.* 1995) show that it has a nearly solar spectrum from the UV to the near–IR (1500Å–10μm): scattering strength is only weakly dependent on wavelength, so that the absorption lines and narrow–band features of the Sun are very accurately reproduced in the ZL. The broad–band color of the ZL is usually described as the ratio of the zodiacal to the solar spectrum as a function of wavelength,

$$C(\lambda,\lambda_0) = \frac{I_{ZL}(\lambda)/I_\odot(\lambda)}{I_{ZL}(\lambda_0)/I_\odot(\lambda_0)}, \qquad (1)$$

in which the reference wavelength, λ_0, is typically around 5500Å. Observations of the ZL to date find $C(\lambda,\lambda_0)$ changing by only 5% per 1000Å at the ecliptic orientation and scattering angles of interest to us.

The solar–type spectrum of the ZL is readily explained by Mie scattering theory, which describes the scattering of light off solid particles larger than the wavelength of the incident light. It predicts the mild wavelength dependence for scattering by particles with the composition and size distribution of the interplanetary dust (IPD) cloud (see Röser & Staude 1978, Berriman *et al.* 1994, and Leinert *et al.* 1998 for a recent summary). Because the equivalent widths of the solar Fraunhofer lines are known with high accuracy, we can uniquely determine the continuum level (mean flux) of the ZL at a given wavelength using the apparent equivalent width of the Fraunhofer lines in the ZL spectrum. However, high signal–to–noise spectra at $\sim$ 1Å resolution are required to measure Fraunhofer lines in the spectrum of the ZL. At the time of these observations, such data could only be obtained from the ground. We therefore measured the absolute flux of the ZL using spectrophotometry between 3900–5100Å obtained at Las Campanas observatory simultaneously with the November 1995 HST observations. To identify the ZL flux over the full wavelength range of the HST observations, we combine these observations with an estimate of the ZL color obtained from the HST and LCO data together, as described in §9. The measurement of the ZL is presented in full in Paper II. In §11, we discuss the use of those results in the EBL detection we present here.

2.3. *Discrete Stars and Diffuse Galactic Light (DGL)*

The Galactic contribution to the diffuse night sky comes from discrete stars, starlight scattered off interstellar dust, and line emission from the warm interstellar medium. Light from resolved stars near the optical axis of the telescope can also scatter into the field of view.

In some previous attempts to measure the optical EBL, even light from discrete, resolved stars was difficult to subtract due to poor detector resolution (e.g. Dube *et al.* 1979, Toller *et al.* 1983). In HST/WFPC2 images, however, Galactic stars in the field can be easily identified and subtracted, with negligible residual contribution to the errors in our final results.

Guhathakurta & Tyson (1989, hereafter GT89), Murthy *et al.* (1990), and others have demonstrated that thermal IR emission from Galactic dust and the scattered optical flux are well correlated, as both are a function of the column density of dust and the strength of the interstellar radiation field which both heats the dust and is scattered by it. We therefore used the IRAS 100μm maps to select a field with low 100μm emission to ensure that the diffuse galactic light (DGL) contribution would be minimal. The approximate 100μm flux in the surrounding

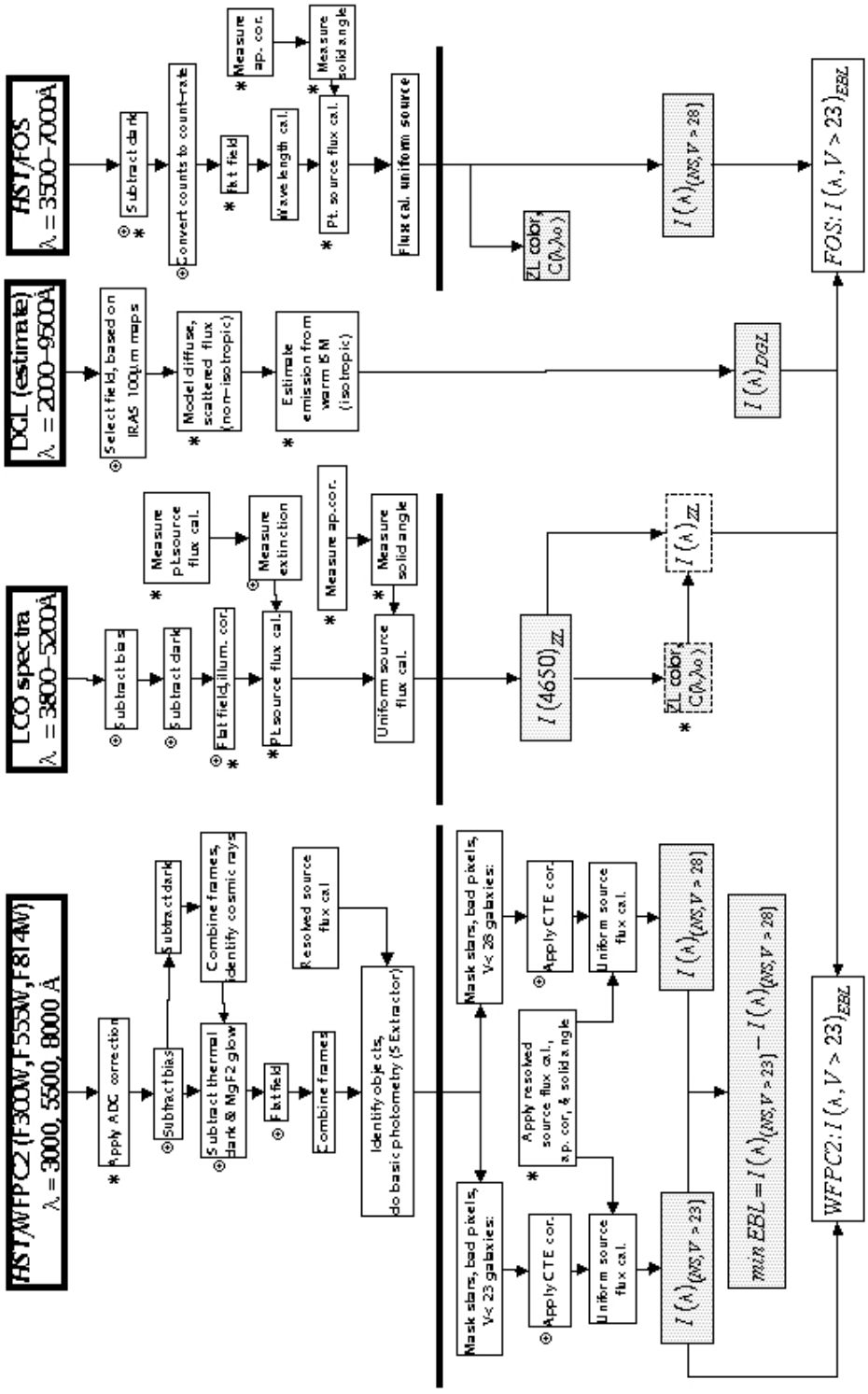

FIG. 2.— Flow chart of data reduction, analysis, and results from all data sets used to measure the EBL. Where appropriate, subscripts to $I(\lambda)$ indicate the bright magnitude cut–off applied. The thick, horizontal bars divide the pre-reduction and analysis steps. The symbols $*$ and $\oplus$ marking steps in data reduction indicate that a systematic or statistical uncertainty is accrued at that step. Normal type–face indicates STScI pipeline data reduction procedures; bold type–face indicates original procedures which we developed for this work. Dashed boxes mark estimates of the ZL color; shaded boxes indicate results derived from one data set alone; thick–lined boxes indicate final measurements of the EBL from combined WFPC2/LCO and FOS/LCO data sets.

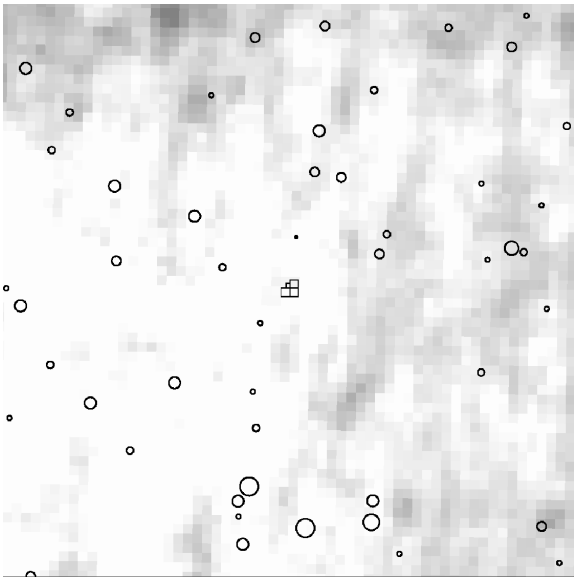

FIG. 3.— *IRAS* 100 μm map (Beichmann *et al.* 1986) covering $1.5° \times 1.5°$centered on the WFPC2 EBL field. The grey–scale is linear: white indicates 0.6 MJy sr^{-1}at 100 μm, corresponding to N(HI)$\sim 0.6\times10^{20}$ and E($B-V$)$\sim$ 0.01 mag; black indicate 1.6 MJy sr^{-1}, corresponding to N(HI)$\sim 1.6\times10^{20}$, E($B-V$)$\sim$ 0.03 mag (see Berriman *et al.* 1994). HST/WFPC2 and FOS footprints are overlaid. Stars with $7 < V < 12$ mag are marked with circles whose radii are linearly proportional the magnitude of the stars.

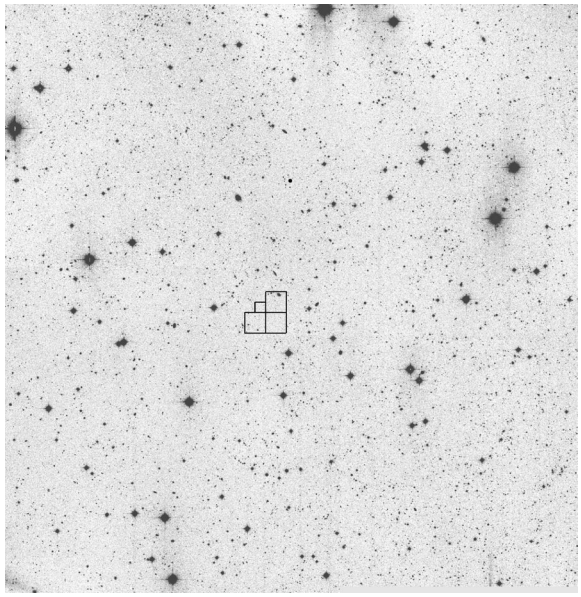

FIG. 4.— The HST/WFPC2 and FOS footprints overlaid on a mosaic Gunn-r–band image ($0.6° \times 0.6°$) taken with the 1m Swope Telescope at the Las Campanas Observatory.

$1.5° \times 1.5°$ region of our observations is shown in Figure 2.3, in which the position of our target field is shown by the HST WFPC2 and FOS footprints overlayed the IRAS 100μm map. We have estimated the low–level DGL (which contributes even along the most favorable lines of sight) by using a simple scattering model which accurately reproduces the observed scaling relations between 100μm thermal emission and the optical scattered light (see Equation 4). The model combines an estimate of the dust column density based on 100μm emission with empirical values for the interstellar radiation field and dust scattering parameters. Unlike the ZL, the flux from DGL is only roughly equal to the EBL in surface brightness, so that uncertainty in this modeling does not prohibit a detection of the EBL.

3. FIELD SELECTION AND HST SCHEDULING

We chose the HST/WFPC2 field (see Table 1 for coordinates) at an ecliptic latitude $|\beta| > 30°$ (to minimize contributions from ZL) and near the Galactic pole in a region of low Galactic 100μm emission (to minimize diffuse Galactic light). We also selected the field to avoid bright stars, in an effort to minimize the scattered light from stars near the optical axis of the telescope. The positions of stars relative to our field can be seen in the r-band CCD image shown in HST Figure 3 and in the IRAS map in Figure 2.3. No stars brighter than 12 AB mag fall within 10 arcmin of the center of our field, and no stars brighter than 7 AB mag fall within 2.5 degrees. Based on measurements of the point spread function (PSF) of HST done with WFPC1, the attenuation factor at 1 arcmin from the center of a point source is 10^{-8} (STScI Technical Memos RSB–85–03, RSB–85–02, ISR/OTA 06.1). Furthermore, the "large–angle" (> 3 arcsec) scattering is roughly one order of magnitude lower for WFPC2 than for WFPC1. Based on these results, the total contribution from stars closer than 5 arcmin to the field is at most 10^{-9} of their total flux, which amounts to one 35 mag star on–axis. The EBL signal, by comparison, is approximately 27.5 mag arcsec^{-2}. The flux from off–axis sources is therefore an insignificant contribution to the background and a negligible source of error.

The exact scheduling of exposures was also critical to this program, as stray solar and terrestrial light in HST observations are a strong function of the orbital position of the satellite. Sunlight scattered off the limb of the Earth can increase the background level by a factor of 10 when the bright limb is near the optical axis of the telescope. All of our science observations were therefore scheduled to execute exclusively in the shadow of the Earth. Because our field was at a viewing angle angle greater than 135° from the Sun during the months of our observations, the satellite was pointed in a direction greater than 45° away from the satellite's direction of motion when our field was observed from within the Earth's shadow. This guaranteed that no upper–atmosphere glow from the satellite's flight path would affect our observations. Scattered moonlight was also explicitly avoided by exposing only with the Moon greater than 65° from the optical axis of the telescope, which is the angular separation at which models predict that the attenuation function for off–axis scattered light becomes flat (STScI Technical Memo RSB–85–03). Based on those models, confirmed by on–orbit measurements (Burrows 1991, Hasan & Burrows 1993), the light from the moon at 65° from the optical telescope assembly (OTA) is less than 10^{-5} photons s^{-1} arcsec^2 per 100Å, which is 1000 times smaller than the lower limit expected for the EBL, and is therefore also a negligible source of background during our observations.

Our 18 orbits were divided into three visits, staggered

TABLE 1
EBL FIELD COORDINATES

System	longitude	latitude
Equatorial(J2000)	$3^h00^m20^s.40$	$-20°10'45''.3$
Galactic	206°.6	-59°.8
Ecliptic	35°.5	-35°.5

by one month each between October and December, 1995. The ZL flux changes with the Earth's orbital position about the Sun and the line of sight through the interplanetary dust during the three visits. We therefore expected to see changes in the total sky flux between visits, at a level predicted by the models of the interplanetary dust. During all three months, our target field has a ZL surface brightness which is within 20% of the absolute minimum intensity of the ZL at any orientation. By separating the orbits for this program into three visits, we were also able to observe the field at two different roll angles – V3 position angle 222° for the November and December visits, V3 angle 132° for the October visit — thereby changing the position of the off–axis stars with respect to the OTA. This allows us to further rule out significant off-axis scattered light and other possible photometric anomalies.

4. HST/WFPC2 DATA

4.1. *Observations*

The 18 orbits scheduled for this program executed on 28 October, 29 November, and 16 December, 1995. During each orbit, a single long integration (1800 sec) was taken while the satellite was in the Earth's shadow and one additional short integration (300–400 sec) was taken to fill the time between target acquisition and entry into the Earth's shadow. Two orbits per visit were spent observing with each of three WFPC2 filters (F300W, F555W, and F814W). The short exposures were combined and used to improve cosmic ray rejection. In all, five 1700 sec darks and ten bias images were taken during the bright portion of the six orbits comprising each visit. The gain setting for these data was $7\,e^-$/DN (bay 4) and the read noise was roughly $5.2\,e^-$ for each of the four CCDs. The field of view of each WFPC2 image is roughly 4.4 arcmin^2 (725×725 well–exposed pixels in each of the 3 WF CCDs, with 0.0996 arcsec^2 per pixel).

4.2. *Basic Data Reduction and Calibration*

The reduction of these data involved a mixture of the standard pipeline and our own methods. The pipeline procedures used included the corrections for analog–to–digital conversion errors, overscan subtraction, bias image subtraction, flat–fielding, and point-source calibration. The accuracy of these steps is largely provided in STScI documentation. Whenever possible, we have independently verified the errors we quote. All steps in the reduction are indicated in the flow chart in Figure 2.1 with associated errors explicitly included in our error budget. The reduction is discussed briefly below; greater detail can be found in Bernstein (1998). The following section should be read by those who are interested in the reduction procedures and detailed error discussions. As the goal of these observations is an *absolute* measurement of the total flux of the night sky, zero point calibration is as critical to the accuracy of the results as flux calibration. Table 3 summarizes the errors discussed below and indicates the dominant sources of error.

4.2.1. *Pipeline*

The WFPC2 analog–to–digital conversion (ADC) has a bias towards DN values which correspond to the setting of all low–order bits in the digitization, with larger signal levels being more strongly affected. The correction for this bias involves replacing the output value with a value corresponding to the scaled average input signal for that output. DN values in the range of our data have an average additive correction of 0.86 DN, with the correction smoothly varying for levels in this range. The same correction is used for each of the four CCDs in WFPC2. The data used to determine this correction were taken pre– and post–dynamic testing, with only 0.02 DN variation. The correction is thought to be stable under normal usage and insensitive to temperature fluctuations (STScI Technical Memo RSB–85–01). At the signal levels of our data, the error after the ADC correction applied is 0.02 DN.

The bias level was removed with a two–step process of overscan subtraction and bias–image subtraction. We employed the usual method established for WFPC2 data of subtracting overscan from odd and even columns using the overscan from each individual exposure. For bias–image subtraction, we used the "superbias" frames produced for the reduction of the Hubble Deep Field (HDF, see Williams *et al.* 1996). This bias frame was produced from the average of 200 frames, and has lower read noise than we could achieve using the 30 bias frames taken during our orbits. Instead, bias frames from our orbits were test–reduced (overscan and bias subtraction using the HDF superbias) to verify that the superbias produced corrected levels consistent with zero, with a scatter of 0.002 DN. As this error is inseparable from our estimate of the error in the dark subtraction, it is included with the dark subtraction in our error budget.

We used the pipeline flat–fielding images provided by the WFPC2 GTO team in May 1996. The pixel–to–pixel flux error in those images is reported in the WFPC2 Data Handbook (V3.0) to be roughly 0.3% (*rms*) for the WF chips, and 0.5% for the PC1. The errors over spatial scales greater than 10 arcsec are less than 0.5% for all four chips. As we excluded data within 75 pixels of the edge of each chip from our analysis, issues of geometrical distortion and vignetting are avoided. The photometric calibration of WFPC2 is tied to the mean level of the flat–fielding images, so that no systematic error is introduced due to flat–

TABLE 2
SAMPLE OF V_{555} SOURCE CATALOG

ID#	x	y	RA(h:m:s)	Dec(h:m:s)	$m_{\rm tot}$	$\sigma(m_{\rm tot})$	$m_{\rm iso}$	$\sigma(m_{\rm iso})$	$A_{\rm iso}$	a	elong.
EBL555-2-1	129	55	3:00:21.66	-20:10:37.4	25.51	0.04	25.45	0.05	11	0.53	1.08
EBL555-2-2	483	55	3:00:24.14	-20:10:35.4	25.94	0.10	26.06	0.09	20	1.72	2.04
EBL555-2-3	623	58	3:00:25.13	-20:10:35.1	26.32	0.13	26.37	0.10	16	1.50	2.03
EBL555-2-4	74	60	3:00:21.28	-20:10:38.2	27.79	0.26	28.27	0.31	3	0.68	1.57
EBL555-2-5	600	61	3:00:24.97	-20:10:35.4	26.62	0.13	26.71	0.12	11	1.04	1.43
EBL555-2-6	279	63	3:00:22.72	-20:10:37.3	27.12	0.17	27.09	0.15	9	0.83	1.15
EBL555-2-7	298	57	3:00:22.85	-20:10:36.6	25.46	0.20	26.16	0.11	29	4.81	7.60
EBL555-2-8	306	65	3:00:22.91	-20:10:37.3	27.47	0.24	27.73	0.23	6	1.08	3.65
EBL555-2-9	155	68	3:00:21.85	-20:10:38.5	26.60	0.12	26.70	0.12	10	0.95	1.29
EBL555-2-10	302	69	3:00:22.88	-20:10:37.7	27.22	0.34	27.70	0.23	7	1.15	2.62
EBL555-2-11	650	68	3:00:25.32	-20:10:35.9	25.09	0.05	25.08	0.05	33	1.30	1.09
EBL555-2-12	756	70	3:00:26.06	-20:10:35.7	25.60	0.12	25.93	0.10	34	2.33	1.53
EBL555-2-13	380	75	3:00:23.43	-20:10:37.9	26.75	0.12	26.70	0.11	9	0.79	1.25
EBL555-2-14	393	74	3:00:23.53	-20:10:37.8	27.42	0.21	27.40	0.17	7	0.82	1.39
EBL555-2-15	729	75	3:00:25.88	-20:10:36.3	27.24	0.20	27.51	0.20	7	0.92	1.67
EBL555-2-16	680	77	3:00:25.54	-20:10:36.7	26.87	0.17	27.29	0.17	9	1.15	1.85
EBL555-2-17	759	82	3:00:26.09	-20:10:36.8	27.79	0.49	28.22	0.33	4	0.95	1.76
EBL555-2-18	534	85	3:00:24.52	-20:10:38.1	25.83	0.12	26.22	0.11	28	1.79	1.31
EBL555-2-19	86	89	3:00:21.37	-20:10:40.9	27.05	0.19	27.22	0.16	8	0.93	1.41
EBL555-2-20	178	95	3:00:22.02	-20:10:41.0	26.72	0.17	26.97	0.15	10	1.15	1.35
EBL555-2-21	96	98	3:00:21.45	-20:10:41.8	27.56	0.23	28.02	0.28	4	0.72	1.45
EBL555-2-22	670	100	3:00:25.48	-20:10:39.0	27.19	0.23	27.56	0.22	10	0.94	1.21
EBL555-2-23	321	100	3:00:23.03	-20:10:40.7	26.30	0.12	26.76	0.14	13	1.16	1.51
EBL555-2-24	276	105	3:00:22.71	-20:10:41.4	27.72	0.28	27.81	0.21	6	0.75	1.71
EBL555-2-25	599	106	3:00:24.98	-20:10:39.8	27.07	0.21	27.31	0.18	10	1.02	1.40
EBL555-2-26	213	107	3:00:22.27	-20:10:42.0	25.91	0.13	26.32	0.11	24	2.19	1.93
EBL555-2-27	666	112	3:00:25.45	-20:10:40.1	26.98	0.21	27.31	0.19	9	1.32	3.09
EBL555-2-28	311	113	3:00:22.96	-20:10:42.1	27.48	0.23	27.80	0.21	6	0.94	2.00
EBL555-2-29	645	106	3:00:25.30	-20:10:39.6	22.01	0.01	22.01	0.01	375	4.82	1.46

NOTE: Coordinates are J2000. Total magnitudes ($m_{\rm tot}$), isophotal magnitudes ($m_{\rm iso}$), and the associated *rms* errors (σ) are in AB magnitudes. The isophotal area ($A_{\rm iso}$) and flux–weighted, second order moment along the major axis (a) are in units of WF pixels, which are 0.0996 arcsec on a side. The isophotal, weighted elongation (e) is the ratio of the second order moments along the major and minor axes, as calculated by SExtractor.

fielding.

4.2.2. *Subtraction of Dark Backgrounds*

We have developed a new method for dark subtraction because the pipeline subtraction ignores the fact that the signal which accumulates on the WF chips while the shutter is closed varies between 0.5–1.1 DN per 1800 sec exposures for the WF3 and WF4 chips (more for WF1, less for WF2). This variability is not caused by thermal dark current, but rather by variations in the dark "glow" contributed by the MgF_2 field–flattening lenses, positioned immediately above each of the WFPC2 chips. When struck by even low–energy (200–2000 eV) ions and electrons (which are abundant in the upper atmosphere in the form of N_2^+ and cosmic rays), MgF_2 will produce broad–band fluorescence on a time–scale << 1 sec (Qi *et al.* 1991). We have found that the cumulative flux in cosmic ray hits recorded in a dark (shutter–closed) exposure correlates strongly with the mean dark level in that frame. This correlation is shown Figure 4.2.2 in which we plot the cosmic ray flux and dark glow for each WFPC2 CCD in each of 15 dark exposures. The scatter around the linear fit for each chip is ~ 0.06 DN. This plot also shows clearly that the dark background in a 1700 sec exposure can vary by as much as ± 0.35 DN. As the total background sky signal through the F300W is only 0.3 DN/1700 sec, accurate subtraction of the dark glow is essential for this measurement.

In collaboration with H. Ferguson (STScI), we developed a method which uses the correlation between the MgF_2 glow and the flux in cosmic rays to isolate the thermal dark component from the dark glow. We obtained a final dark solution using 80 individual dark images taken between October and December 1995, and have tested the accuracy of this method by test-reducing the 15 dark exposures taken between the science exposures of our program. These 15 darks were not used in determining the dark solution itself. After ADC correction, overscan subtraction, bias subtraction, and dark subtraction by the prescription described above, the average mean level of the 15 darks is consistent with zero, with a scatter of < 0.05 DN per 1700 sec exposure. The statistical error in the pipeline dark-subtraction, by comparison, is roughly 0.15–0.25 DN for the WF3.

4.2.3. *Charge Transfer Efficiency (CTE)*

Accurate photometry depends on stable charge transfer efficiency (CTE), which is the efficiency with which electrons are transferred between pixels during read out. Variable CTE as a function of total charge level, time, or position over the chip results in non–linear sensitivity. Unfortunately, the WFPC2 chips are known to have a "a small parallel CTE problem" (Holtzman *et al.* 1995b, henceforth H95b; Whitmore, Heyer, & Casertano 1999): the percentage of electrons which are read–out of a pixel depends on the row number of the pixel in question, the number of electrons in that pixel when read–out begins, and the mean charge level in the pixels through which the charge travels during read–out.

Based on in–flight point source photometry and on laboratory tests using a CCD from the same silicon wafer as WFPC2 CCDs, the CTE variability is known to be caused

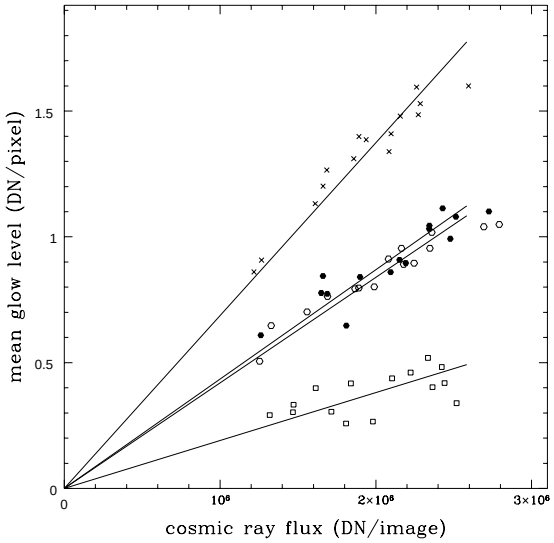

FIG. 5.— Correlation between the cumulative flux in cosmic ray events and the mean dark level (thermal dark plus MgF_2 glow) for each WFPC2 chip in 15 exposures: ×'s for PC1 fluxes, open boxes for WF2, circles for WF3, and filled circles for WF4. Statistical errors in both quantities plotted are negligible; scatter in the correlation probably reflects statistical variations in the energy level of the cosmic rays hitting the CCD and the MgF_2 plates.

by electron traps which were in the silicon itself before the pixel mask was etched into the wafer (J. Trauger, private communication). Although electrons can be trapped in the silicon at the pixel where they are detected, a greater surface area of silicon is encountered during read–out, providing greater opportunity for trapping if the traps are not already filled before readout begins. When a bright point source is imaged against a faint background, many new traps are encountered during read–out. For example, 4% of a 10,000 e^- point source are lost when the charge is transferred over 800 rows if the background level is ~10 e^-/pixel. If the traps are already filled by a high background level over the whole chip, fewer electrons will be lost from sources during read–out. Surface photometry is less affected by this CTE problem because all pixels are filled to the same charge level and, hence, new traps are not encountered during read-out.

The signal level read out for our images is roughly 80e-/pixel for the F555W and F814W images and 2e-/pixel for the F300W images. We have identified the CTE losses in these data by two methods. First, data from WFPC2 and laboratory tests conducted by J. Trauger of point sources show that $\sim 0.35\, e^-$/pixel are lost from a point source which is imaged against a background level of roughly $80\, e^-$/pixel, while $\sim 1.1\, e^-$/pixel are lost when the background level is zero (J. Trauger, private communication). The difference between the number of electrons lost at the two different background levels indicates that the number of single–electron traps available in a uniform background of $80\, e^-$/pixel is $0.75\, e^-$/pixel (~1.1-0.35). Second, to confirm that this trapping reflects the CTE losses for uniform sources, we have conducted another set of tests with the help of J.Trauger to measure the non-linear response of the spare WFPC2 CCD to uniform, low–level backgrounds.

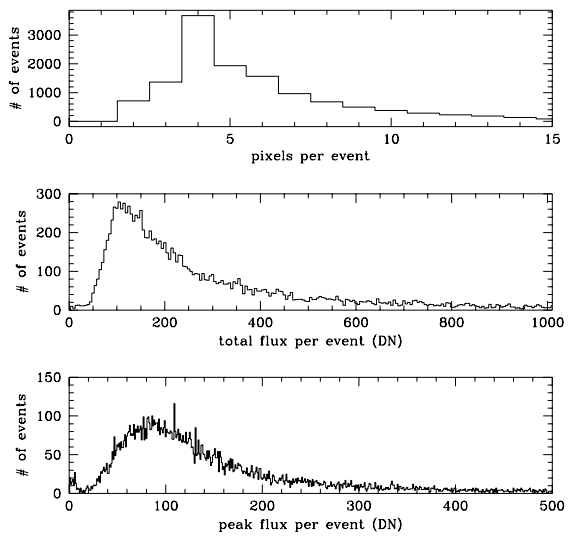

FIG. 6.— Histogram of cosmic ray events as a function of the number of affected pixels (top panel), total flux (middle panel), and peak flux (bottom panel). The number of events falls off in each plot before an event would become difficult to detect in these data.

In this test, we simply expose the CCD to a light source which is stable to better than 0.1% for varying lengths of time and look for non-linearities in the detection rate. The results of these uniform-source test are in excellent agreement with results from point–source tests. We therefore conclude that 0.75 ($\pm$0.25) e^-/pixel are lost when a mean level of $\sim 80\,e^-$/pixel are read-out, and 0.1 ($\pm$0.05) e^-/pixel are lost from a mean level of $\sim 2\,e^-$/pixel. The maximum uncertainty in these corrections is a negligible contribution to our final results (see Table 3). For more detail on the result of the laboratory tests, see Bernstein (1998).

4.2.4. *Cosmic Ray Detection*

If low–energy cosmic ray events were left unidentified in WFPC2 data, we would unintentionally include the signal from those events in the inferred background level. Figure 4.2.3 shows the total number of cosmic ray events as a function of total flux, peak flux, and affected pixels per event. In each histogram, the number of cosmic ray events falls off sharply well before cosmic rays would become difficult to detect: both peak and total fluxes for cosmic ray events are significantly higher than the mean level of the background ($\lesssim$ 10 DN), and the total number of pixels affected by a single cosmic ray event rarely drops below three. We therefore conclude that the cosmic ray removal process detects virtually all cosmic rays which hit the chips.

4.2.5. *Flux Calibration*

The final accuracy of a surface brightness measurement depends on four independent facets of the calibration: point source calibration; aperture correction, compensating for flux not recovered in the point source calibration; the calibration of the fiducial standard star system; and the solid angle subtended by each pixel. The solid angle of the pixels is, of course, very well known and is a negligible source of error for the WFPC2 data. However, the other three calibration steps require quantities of data and observing time only available to the WFPC2 Instrument Team. Details of the WFPC2 calibration are thoroughly discussed in Holtzman *et al.* (1995a, henceforth H95a), H95b and subsequent STScI Instrument Science Reports. Below, we summarize their results.

Sensitivity to the same fiducial standard is stable to $\sigma < 1\%$ for the F555W filter, and $\sigma < 1.5\%$ for the F814W and F300W between February 1995 and March 1997 (STScI TIR/WFPC2 97–01). Observations of the same standard may be variably affected by CTE due to variations in the peak flux of the observation which will arise from variations in the position of the PSF within a single pixel. The real response of WFPC2 is, therefore, likely to be more stable than this result. The synthetic photometry package (SYNPHOT), including system throughput curves and synthetic zero–points, is based on the HST secondary standard system and is estimated by H95b to be accurate for point sources to roughly 1% for a source with typical stellar colors. Point–source calibration should therefore be good to roughly 1%.

Aperture corrections based on the encircled energy curves are given in H95a (see Figures 5a & 5b, and Tables 2a & 2b in H95a). For the optical filters, the aperture correction is nearly 10% in moving from a 0.5 arcsec aperture to an infinite aperture, with uncertainties of 1% for the redder bandpasses, and 1-2% for the F300W.

Finally, the secondary standard star system which is used for all the HST instruments is "conservatively estimated" to be within 1% of the Hayes 1985 optical calibration of Vega (Bohlin 1995; Colina & Bohlin 1994; Hayes 1985), with internal agreement of the same order. The agreement between the HST secondary system and the Hamuy *et al.* (1992) secondary system to which our ground-based observations are tied is estimated to be 1–2%, as discussed in Paper II.

4.3. *Combined Images*

We produced combined images in which individual resolved sources could be identified and photometered for two purposes: (1) to allow bright galaxies and stars to be identified and excluded from the EBL measurements, (2) to allow comparison of the galaxy sample and EBL results to other data sets. The measurements of the mean sky flux discussed in §5 and §10 are obtained from individual WFPC2 exposures. The deepest combined image for each filter is obtained from the four exposures taken during the November and December visits, during which the telescope roll angles were the same. The small differences in the alignment of the WF CCDs prevent data taken during the October visit from being usefully included in combined images for the purposes of accurate photometry. The combined images and resolved source catalogs are available on the NASA/IPAC Extragalactic Database (NED).[2] A sample of the catalogs is shown in Table 2 and the combined F555W image is shown in Figure 4.3 The F300W, F555W, and F814W catalogs contain 140, 687, and 644 objects, respectively. The photometry of these sources is discussed in the next subsection.

[2]Web address: http://nedwww.ipac.caltech.edu/level5/

TABLE 3
WFPC2 BACKGROUND FLUX: ERRORS PER IMAGE

	F555W, F814W	F300W
Statistical (per image)		
Off–axis scattered light (§3)	< 0.001 DN	< 0.001 DN
Dark and bias subtraction (§§4.2.2, 4.2.1)	± 0.05 DN	± 0.05 DN
Flat–fielding (§4.2.1)	...	...
CTE (§4.2.3)	± 0.03 DN	± 0.007 DN
Cumulative Statistical Error[a]	0.06 DN	0.05 DN
Systematic		
A–to–D conversion[b](§4.2.1)	± 0.02 DN (0.2%)	± 0.02 DN (6%)
Point source flux cal.(§4.2.5)	1%	1.5%
Aperture correction (§4.2.5)	1%	1%
Solid angle (pixel scale)(§4.2.5)	0.1%	0.1%
Combined Systematic Error[c]	1.2%	5.6%

[a]Individual random errors have been added in quadrature to obtain a cumulative, one-sigma random error in DN. To obtain fractional errors, compare to the mean flux per exposure ($\sim$0.3 DN per pixel for the F300W, $\sim$12.5 DN per pixel for F555W and F814W).

[b]The A–to–D conversion is an additive correction, the associated error is therefore the ratio of the A–to–D error and the mean level in the frame. All other systematic uncertainties listed are multiplicative.

[c]Systematic errors have been combined assuming a flat probability distribution for each contributing source of error. The resulting systematic error is roughly Gaussian distributed, and the quoted value is the 68% confidence interval. For a detailed discussion see §11.

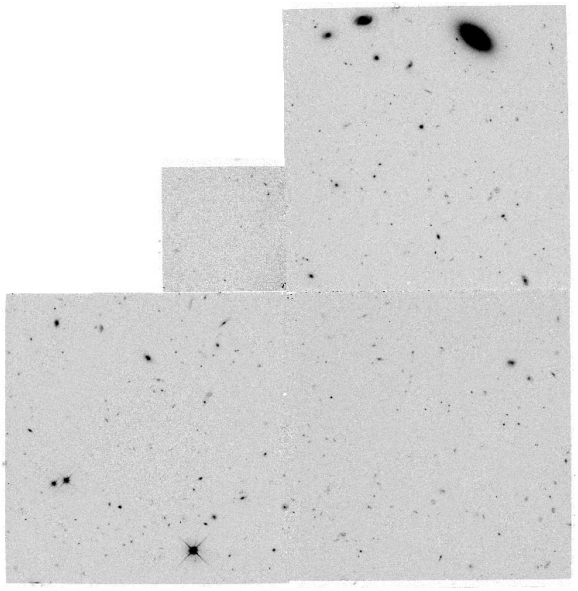

FIG. 7.— The combined F555W images from November and December visits. The total exposure time is 4×1800 sec.

4.4. *Resolved Objects*

We used the image analysis package SExtractor (Bertin & Arnouts 1996) for object identification and photometry. The requirement for detecting an object in our data is a core surface brightness, $\mu_{\rm core}$, of at least $2\sigma_{\rm sky}$ within the core 4 pixels. The isophotal detection threshold, $\mu_{\rm iso}$ was defined as $1.5\sigma_{\rm sky}$ over 6 pixels, after smoothing with a 3×3 boxcar filter. This corresponds to isophotal detection thresholds of 24.7, 25.8, and 25.3 ST mag arcsec^{-2}, at F300W, F555W, and F814W, respectively. The shape of the smoothing kernel and the detection threshold have little affect on detection of objects with $V_{555} < 27.5$ AB mag, and photometry is not strongly affected for objects with $V_{555} < 27$ AB mag. Total magnitudes are defined as the flux within an area at least three times larger than the ellipse defined by the first moment radius (see Kron 1980) and isophotal elongation. For well–detected sources, the detection and photometry parameters we employ are similar to those used by the HDF team in producing the HDF catalogs (see the photometry discussion in Williams *et al.* 1996). Isophotal detection limits are roughly 1.5 mag brighter than the HDF, in keeping with the difference in exposure time, which is a factor of $15 - 21$ in the various bandpasses. Differential number counts for our field are plotted in Figure 4.4. Our detection limits are illustrated by the turn–over in the counts in each band. The $\sqrt{N}$–error bars show that $V \sim 23$ AB mag is reasonable bright–magnitude cut-off for observations in a field of this size. The galaxy counts from the HDF are also plotted in Figure 4.4 to demonstrate that the field we have observed contains a typical field–galaxy population in both color and number density. The HDF is a convenient benchmark for this comparison simply because the data are publicly available, widely studied, and of a similarly "blank" field. The HDF counts show twice as many galaxies at magnitudes brighter than 23 AB mag in each of the three

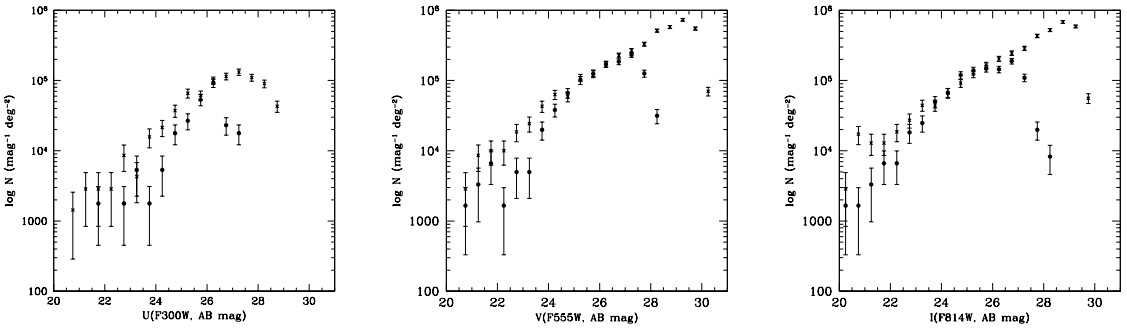

FIG. 8.— Differential galaxy counts with $\sqrt{N}$ error bars from WFPC2 EBL images (filled circles), and the HDF images at F300W, F606W, and F814W (×'s). HDF counts are taken directly from the published catalogs (Williams *et al.* 1996). The difference in completeness limits between the two data sets reflects the difference in total exposure times, which are roughly ×21, ×16, and ×17 at U, V, and I, respectively.

band, while the difference in number density fainter than 23 AB mag is modest. Such differences at bright magnitudes are well within the typical field–to–field fluctuations for galaxy counts and illustrate the need for a bright magnitude cut–off.

Four stars are detected in the WF chips, three in WF2 with $V_{555} = 19.0$, 20.5 and 20.8 AB mag, respectively, and one in WF4 with V_{555} =22.0 AB mag. Star–galaxy separation poses no difficulty; stars brighter than $V_{555} \sim$ 23.0 AB mag are masked out, regardless, and the flux from stars beyond that limit is < 10% of that from detected galaxies at the same apparent magnitudes (Infante 1997).

4.5. *On–Axis Scattered Light*

Scattered light from the "bright" ($19 < V < 23$ AB mag) objects imaged in the field is one possible source of error in a measurement of the background from fainter objects. To quantify this effect, we begin by considering how much light these sources produce relative to the total flux in an image. In Figure 4.5, we plot the ratio of the flux from bright sources to the total flux detected in each of the three WF CCDs during each of four exposures. The total flux is just the sum of all counts in the calibrated images. The flux from bright sources is a background–subtracted flux within four times the isophotal radius ($4r_{\rm iso}$) for galaxies (see §10.1) and within a 5 arcsec radius for stars. For each bandpass, the ratio of flux in bright sources to the total flux varies from chip to chip. In the WF2 or WF3 chips, bright objects contribute only ∼ 5% of the total integrated flux. As several of the brightest galaxies in the field are imaged on the WF4 chip, almost ∼ 15% of the flux in F555W and F814W in that field comes from objects with $V < 23$ ST mag.

In order exclude these $V < 23$ AB mag objects from the measured background, we masked regions around each resolved galaxy which extend to four times the isophotal detection radius of the galaxy, and masked regions with radii of 5 arcsec for stars. Based on the encircled energy curves in H95a and growth curves in our own images (see §10 and Appendix B), we estimate that less than 2% of the light from these objects is imaged beyond the extent of the masked regions. As an upper limit on their scattered light, 2% of the flux from these objects constitutes only 0.1×10^{-9} ergs s^{-1} cm^{-2} sr^{-1} Å^{-1}, less than 3% of the total

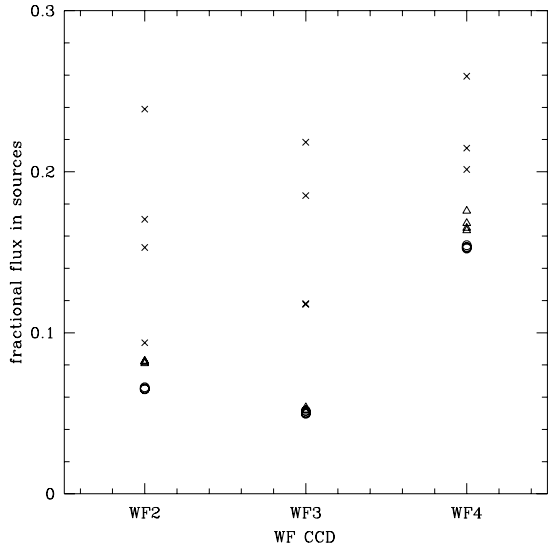

FIG. 9.— The flux from bright ($V_{555} < 23$ AB mag) sources relative to the total flux in each WFPC2, EBL image is plotted for four exposures through three filters (twelve images total). The total flux is just the sum of all counts in the calibrated images. The flux from bright sources is a background–subtracted flux within four times the isophotal radius ($4r_{\rm iso}$) for galaxies (see §10.1) and within a 5 arcsec radius for stars. The F555W, F814W, and F300W flux ratios are marked by open circles (overlapping), triangles, and crosses, respectively.

flux at 5500Å in our estimate of the EBL. As discussed previously in §3, the scattered light from off–axis sources is also negligible.

At the wavelength of the F300W filter, the flux from bright objects on the WF4 chip is 15–20% of the total flux, and variation in the percentage flux contributed by objects in the F300W images is greater than in the other two bands. These characteristics are explained by two facts: (1) errors in dark glow subtraction cause noticeable variation in the background level between exposures in this band; and (2) the ZL falls off rapidly below 4000Å, so that the ZL contribution to this band is a factor of three smaller than in the F555W or F814W and variations in source flux

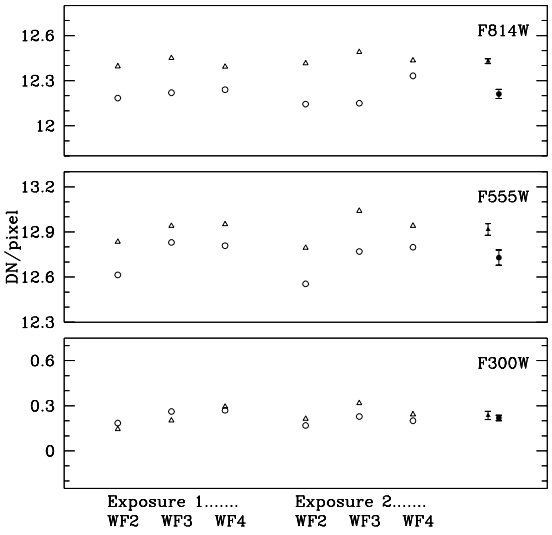

FIG. 13.— Total background detected (DN/pixel in 1800 sec) in each of two exposures per filter obtained in the November (△) and December (○) 1995 visits. Bright galaxies ($V_{555} < 23$ mag), stars, and bad pixels are excluded from this average. Filled symbols indicate the mean for each visit with error bars showing empirical 1σ scatter around the mean, in good agreement with tabulated statistical errors (see Table 3). For this comparison, DN/pixel for each chip has been normalized to match the gain of the WF3 chip (see H95b). Decrease in the mean from November to December is in good agreement with the predicted change in the ZL flux due to viewing geometry.

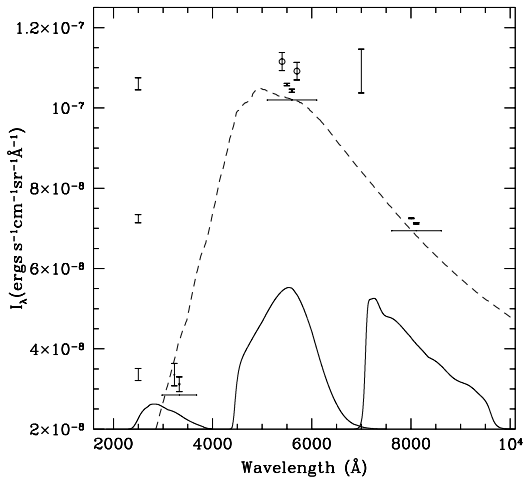

FIG. 14.— The total sky flux detected through each of the WFPC2 filters in the November and December 1995 data sets, excluding bright galaxies ($V_{555} < 23$ AB mag). November 1995 results are indicated at the central wavelength of each filter; the December 1995 data are offset by +100Å for clarity. The dashed line shows the ZL spectrum at the appropriate flux; horizontal bars show ZL flux convolved with WFPC2 bandpass profiles. The total background detected with the FOS spectra are marked by ○'s and offset left (November) and right (December) of the central F555W wavelength. Error bars on all points indicate one–sigma statistical errors (see Tables 3 and 5). The floating error bars, arbitrarily plotted at 2500Å, show systematic uncertainties in the WFPC2 results at the indicated fluxes. The floating error bar at 7000Å shows the systematic uncertainty in the FOS results. Solid curves show the effective F300W, F555W, and F814W bandpass profiles.

from chip to chip are fractionally larger in this band than in the other two. In contrast, ZL contributes roughly 95% of the diffuse background at 5500–9000Å (see §9 and Paper II). Nonetheless, the contribution to the background from detected objects in the F300W images, again assuming 2% scattered light, is still a minor uncertainty in our results, being 0.3×10^{-9}ergs s^{-1} cm^{-2} sr^{-1} Å^{-1}, or 7% of the EBL we detect at 3000Å.

5. HST/WFPC2 TOTAL MEASURED BACKGROUND

After calibration, we measure the total background signal by simply taking the average of the detected flux per pixel, excluding pixels which fall into any of the following three categories: those flagged as bad in the data quality file for any reason (see WFPC2 Data Handbook V3.0), those within two pixels of a cosmic ray event, or those within the masked region associated with a star or galaxy brighter than $V_{555} = 23$ AB mag, as described in the previous section. We show the masked regions in Figures 10–12, for each of the WF chips. Masks were defined based only on the F555W images; the same object masks were applied to all three bandpasses. The detected EBL at all wavelengths is therefore defined by contributions from the same sources.

Each WF image from each 1800 sec exposure produces a measurement of the mean background. We have averaged the six measurements from each visit to obtain a single background measurement from each visit. The results for the November and December 1995 visits are compared in Figure 5 to illustrate the change in background due to the geometric path length through the IPD, and thus the difference in ZL contribution during the two sets of observations. The same modulation in background flux was identified in the FOS data between November and December 1995, as discussed in §7. The predicted change from October to November is of order 10%. However, as there are no FOS or ground–based measurements in October, the interpretation of the modulation as a change in ZL is not conclusive for that epoch. We do not include the PC data in the final average because the dark subtraction is least accurate for that chip due to the smaller pixels and higher dark current (see §4.2.2), and because the field of view of the PC is a negligible increase over that of the other three chips. However, the PC chip gives the same result as the WF chips to within 2%, which is consistent with the variation in object distribution over the 4 chips and dark subtraction errors.

The error bars plotted in Figure 5 show the statistical variation between the six measurements (three WF chips, two exposures per filter) from each visit. This scatter is well matched to the statistical errors that we predict based on our assessment of the errors accrued at each stage in the data reduction (see Table 3). Systematic errors are dominated by the flux calibration from DN to physical units and are not shown in the comparisons in Figure 5 as they are, of course, identical for all points. In Figure 5 we plot the total background flux measured in each bandpass in the November and December visits in physical flux units

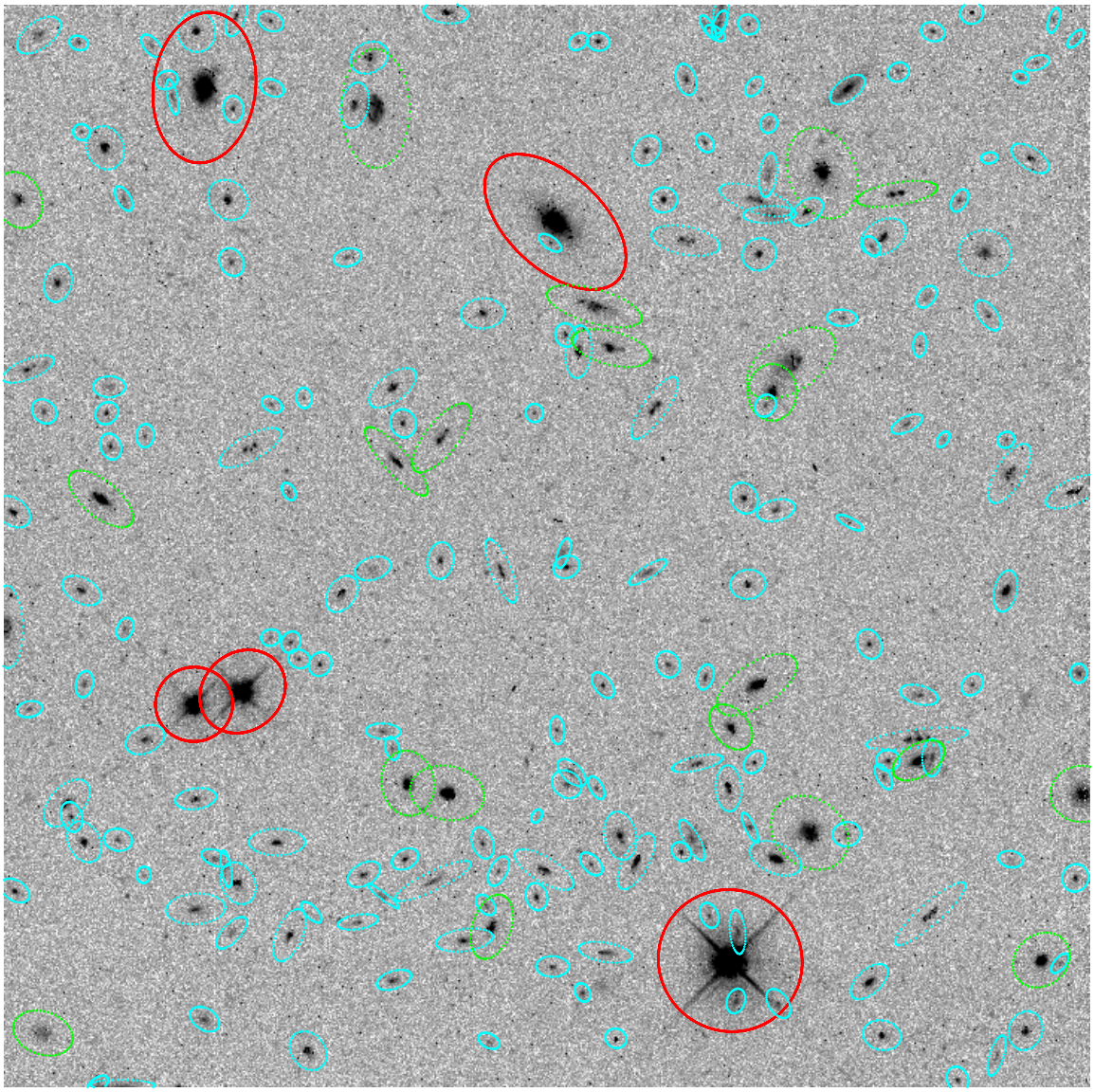

FIG. 10.— Combined F555W WF2 image. North is up and East is left. The ellipses indicate the region extending to 4× the isophotal detection radius, as discussed in §10. Red ellipses mark galaxies with $V_{555} \lesssim 23$ AB mag; green ellipses, $23 < V_{555} \lesssim 25$ AB mag; and blue ellipses, $25 < V_{555} \lesssim 28.5$ AB mag. All sources in the catalog are shown. The completeness limit is $V_{555} \sim 27.5$.

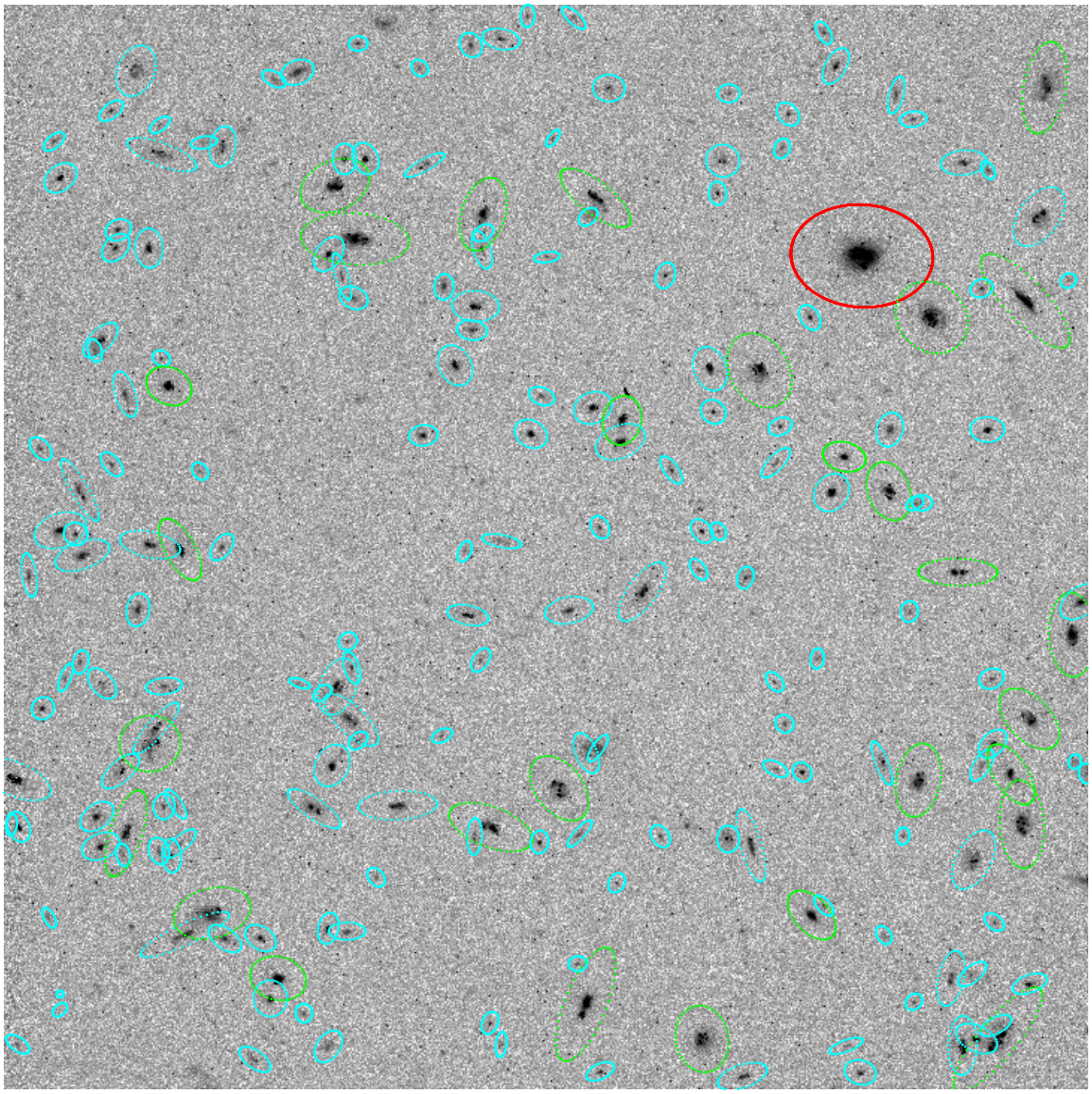

FIG. 11.— Combined F555W WF3 image. North is up and East is left. Ellipses are as in Figure 10.

TABLE 4
TOTAL SKY FLUX (FOREGROUNDS AND EBL) MEASURED FROM WFPC2

Filter	λ_0(FWHM) Å	Total Background	(± *rms*)[a]	[± sys][b]
November 1995				
F300W	3000 (740)	3.35×10^{-8}	(± 9%)	[± 5.6%]
F555W	5500 (1230)	1.06×10^{-7}	(± 0.3%)	[± 1.4%]
F814W	8000 (1490)	7.24×10^{-8}	(± 0.2%)	[± 1.4%]
December 1995				
F300W	3000 (740)	3.12×10^{-8}	(± 7%)	[± 5.6%]
F555W	5500 (1230)	1.04×10^{-7}	(± 0.4%)	[± 1.4%]
F814W	8000 (1490)	7.11×10^{-8}	(± 0.2%)	[± 1.4%]

[a]Statistical errors indicate one–sigma scatter in the six measurements per visit (three images per exposure, two exposures). Compare to estimated errors in Table 3.

[b]Systematic uncertainty as tabulated in Table 3.

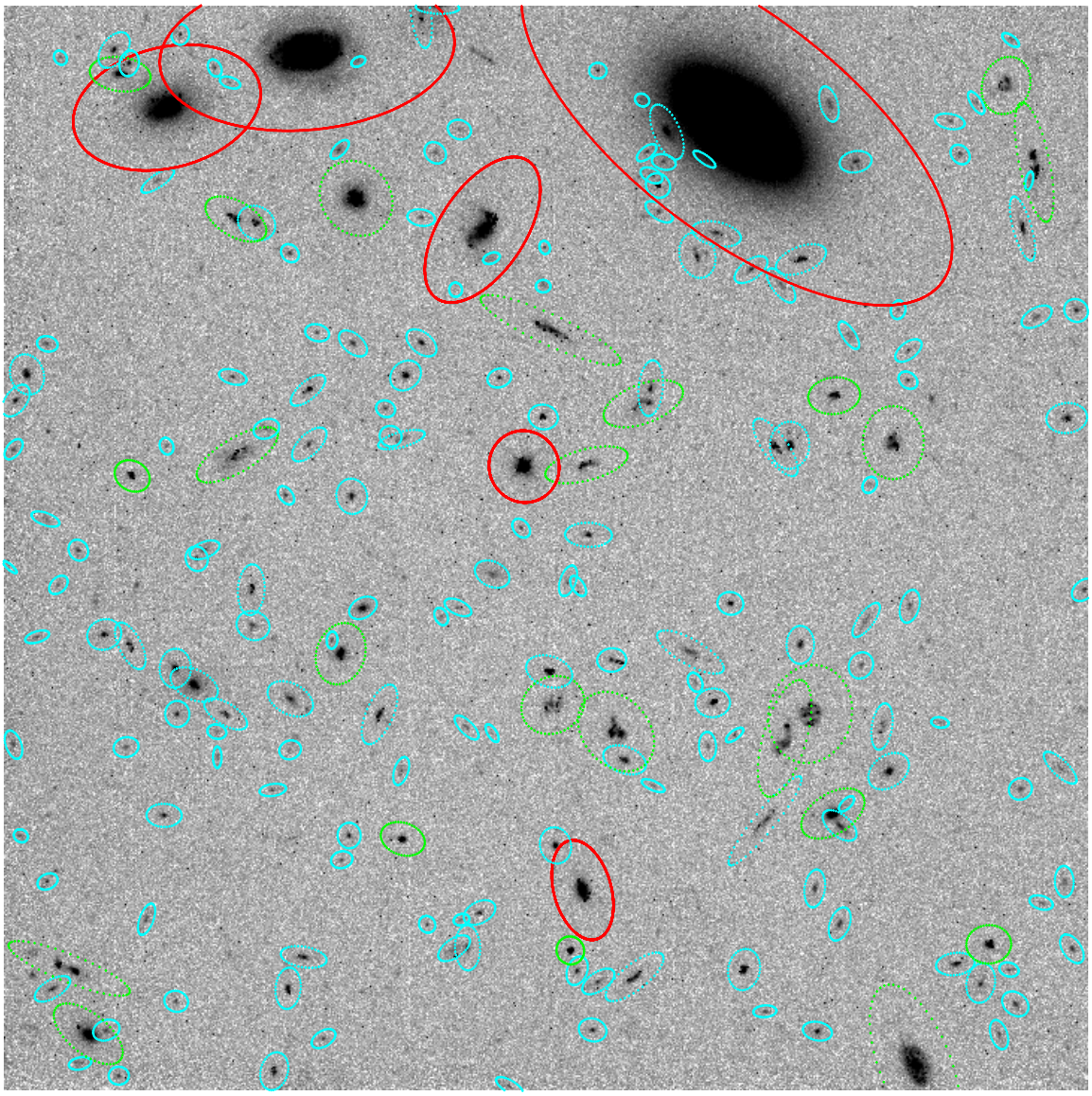

FIG. 12.— Combined F555W WF4 image. North is up and East is left. Ellipses are as in Figure 10.

(ergs s^{-1} cm^{-2} sr^{-1} $Å^{-1}$) with statistical and random 1σ errors plotted separately. The measurements are summarized in Table 4. The zodiacal light spectrum is shown at the flux level we measure in our ground–based spectrophotometry (see §9) to demonstrate that background observed from HST is clearly dominated by zodiacal light.

6. HST/FOS OBSERVATIONS AND DATA REDUCTION

The FOS field of view during our parallel observations is determined by the WFPC2 coordinates and the roll angle of the telescope, which we carefully specified. Ground based images taken with the Swope 1 meter telescope at Las Campanas Observatory were used to assure that the FOS field of view was free of detectable sources brighter than $V = 25$ AB mag.

Based on calculations using an early version of the FOS exposure–time calculator, the FOS/RED was used in parallel observing mode and configured with the 1.0-PAIR aperture and the G570H disperser during our October visit, producing spectra with ~ 4.5Å resolution from 4500 to 6800Å. No exposures were taken during transits of the South Atlantic Anomoly. These data were intended to provide a measurement of the ZL by the method outlined in §2.2, but the count rate from the sky in this configuration was comparable to the instrument dark rate (~ 0.01 DN/sec per diode). Accordingly, the FOS observations during the November and December 1995 visits used the FOS/RED, A–1 aperture (3.66×3.71 arcsec^2), and G650L disperser, which provided spectra with ~ 12 diodes ($\sim$ 300Å) per resolution element for an aperture–filling source (25Å per resolution element for a point source) from 3800–7000Å and a signal–to–noise ratio of almost 20 for the night sky. While narrow–band imaging as such is not useful for measuring the ZL flux by its spectral features, these data do provide better spectral resolution than WFPC2 images, and a second, independent measurement of the total background. We limit our discussion to the data from the November and December visits. One 1300 sec FOS exposure was obtained per orbit during these visits, executing within the time-span of the 1800 sec WFPC2 observations to avoid conflicts in writing the data to on–board recorders.

Many of the pipeline calibration procedures (described thoroughly in the HST Data Handbook) contribute negligible errors for our purposes and were adopted directly. In order of their application, the pipeline procedures used include the conversion from counts to count–rate (CNT_CORR), flat fielding (FLT_CORR), wavelength calibration (WAV_CORR), and flux calibration (AIS_CORR, APR_CORR, and TIM_CORR). The A–1 aperture defines the throughput standard for other apertures, so that the relative correction (APR_CORR) for the A–1 aperture is unity. The G650L has no observed time variation, so that the correction factor applied by the TIM_CORR procedure is also unity. We were able to improve on the dark subtraction procedure, and accordingly used our own methods for that step, as described below. Unfortunately, much of the information needed to obtain accurate surface photometry with the FOS, namely the solid angle of the apertures and PSF of the instrument, has never been provided by STScI. We have therefore supplemented the pipeline calibration with an explicit measurement of the PSF of the instrument. The final flux calibration has a systematic uncertainty of 4.5%. Errors at each step in the calibration are summarized in Table 5, with the total systematic error tabulated as described in §5. Below, we summarize the calibration of the FOS data and briefly discuss the results. Greater detail can be found in Bernstein (1998). Once again, the following section is intended for readers who are interested in the details of the data analysis.

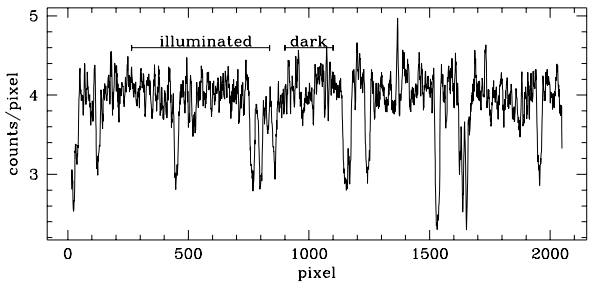

FIG. 15.— Average of 25 FOS dark exposures (1300 sec), demonstrating the stability of the pixel-to-pixel structure of the dark signal. Strong features appear where diodes have been turned off due to poor performance. Sub–stepping along the diodes allows complete spectral coverage over these dead diodes.

6.1. *Dark Subtraction*

The majority of the FOS instrumental background is Cerenkov radiation, caused by cosmic rays striking the photocathode, rather than thermal dark current. Consequently, the instrumental background can vary by factors of two between exposures, a fact ignored in the pipeline calibration. As with the WFPC2, the relative dark rate is a function of instrument geometry and is quite stable over the detector. The G650L low–resolution grating illuminates only 144 of the 512 diodes; therefore, the unilluminated portion can be used to identify the dark rate during a given exposure. On the suggestion of L. Petro (private communication), we produced a "superdark" using 25 dark frames taken in the HDF parallel program (Program 6342, Freedman; Program 6339, Petro) and scaled this to the level indicated by a subset of the unexposed diodes (pixels 900–1100) in each of our spectra. The exposed and unexposed regions of the diode array are labeled in Figure 6.2, where we plot the averaged dark spectrum. To determine the accuracy of this dark–subtraction method, we have reduced darks which were taken during our own orbits expressly for this purpose. The test reduction of these darks shows no systematic error in the dark subtraction by this method, and statistical errors are dominated by shot noise (± 2.2 DN/pixel). The mean dark level can be determined in an individual frame to roughly ± 0.3DN/pixel. With a sky signal of roughly 30 DN/pixel in the low-dispersion configuration, this dark–subtraction method introduces a 0.5% random error to each spectrum overall and 0.4% systematic uncertainty to each resolution element.

6.2. *Flux Calibration*

The surface brightness of an aperture–filling source is a function of the pipeline–calibrated spectrum, $F(\lambda)$ in ergs s^{-1} cm^{-2} $Å^{-1}$, the detector solid angle, Ω, and the

TABLE 5
FOS BACKGROUND FLUX: ERRORS PER RESOLUTION ELEMENT

	Random	Systematic
Poisson noise (§6)	2%	···
Dark subtraction (§6.1)	0.5%	0.4%
Fiducial standards (§4.2.5)	···	1%
Point source flux cal. (§6.2)	···	1.5%
Aperture correction (§6.2)	···	2%
Solid angle (§6.2)	···	2%
Cumulative[a]	(±2.1%)	[± 2.8%]

[a]Statistical errors have been combined in quadrature to obtain a cumulative, one-sigma error. Systematic errors have been combined assuming a flat probability distribution for each contributing source of error. The resulting systematic error is roughly Gaussian distributed, and the quoted value is the 68% confidence interval. For a detailed discussion see §11.

aperture correction, $T(\mathrm{A}{-}1){\times}D$, which includes a term for flux lost at the A-1 science aperture ($T(A-1)$) and at the detector (D):

$$I(\lambda) = \frac{F(\lambda)\ T(\mathrm{A}-1)\ D}{\Omega}. \qquad (2)$$

The pipeline calibration (calibration of the spectrum as appropriate for a point source) depends on the stability of the instrument for relative flux calibration and on the accuracy of the fiducial standards for absolute flux calibration. The accuracy of the secondary standard star system does not dominate the FOS calibration uncertainty; it was already discussed briefly in §4.2.5 and is discussed further in Paper II.

The pipeline calibration converts DN sec^{-1} per diode to ergs sec^{-1} $\mathrm{\AA}^{-1}$, as appropriate for point sources, achieving repeatability of 1–2% for point sources only if they are centered in the aperture to within ±0.2 arcsec (Keyes 1995). This sensitivity to centering implies at least two serious complications for surface photometry. First, the transmission efficiency across the photocathode can vary by as much as 20% over surface areas corresponding to 10 diodes. Second, and more importantly, the PSF is not well contained within either the aperture, the detector, or both. An accurate aperture correction is therefore crucial to surface photometry.

The aperture dilution factor, $T(\mathrm{ap}) \times D$, given in the FOS Instrument Handbook is an estimate produced by modeling based on the OTA with post–COSTAR configuration. While no official Instrument Science Report exists, unofficial estimates for the monochromatic transmission of the A–1, post–COSTAR configuration at 6500Å range from 97% (R. Bohlin, private communication) to 95% (The Data Handbook V3.0). Because this factor is crucial to our result, we have recalculated it using data taken for this purpose as part of the FOS calibration program (Proposal 5262, Koratkar). These data were taken in ACQ/IMAGE mode, which uses no dispersing element, providing a two dimensional image in the diode plane. The stepping pattern used for the observations was kindly provided to us by E. Smith at STScI. Our reduction and analysis of these data are described in Bernstein (1998). We find that 98% of the flux from a point source is contained within the A–1 aperture at the focal plane, and 96.5% of that flux is then imaged onto the 1.29 arcsec spatial extent of the diode array: $T(\mathrm{A}{-}1){=}0.98$ and $D = 0.965$. Thus, we find

$$T(\mathrm{A}-1) \times D + 0.002 \approx 0.95, \qquad (3)$$

in which we have included a small (0.002) correction for conversion from the "white" light of the ACQ/IMAGE data to our central wavelength of 5500Å. The statistical error in this estimation is much less than 1%, but the systematic uncertainty may be as large as 2%.

The A–1 science aperture measures $3.63 \times 3.71\,\mathrm{arcsec}^2$, with 1% errors in both dimensions. In the spatial direction the solid angle is determined by the diodes, which are 1.289(±1%) arcsec in the spatial direction. This values is based on a laboratory measurement made before launch (Instrument Science Report ISR CAL/FOS–019), and has been corrected for the measured change in the FOS plate scale before and after COSTAR was installed (ISR CAL/FOS–123,141). The effective solid angle through the A-1 aperture is then $3.63{\times}1.29\,\mathrm{arcsec}^2$, or $4.68\,\mathrm{arcsec}^2$ with an uncertainty of $\sim 2\%$.

7. HST/FOS: RESULTS

The combined averages of the six spectra taken during the November and December visits, respectively, are shown in Figure 7. With roughly 80 counts per diode, and twelve diodes per resolution element, the statistical error per resolution element for one spectrum is roughly 4%. Statistical errors in the averaged spectra are roughly 1.5–2%, indicated by the error bars which are placed one per resolution element (300Å). The dark subtraction contributes an error of less than 0.5%. We do not show systematic uncertainties, as they will affect both November and December data in the same way and are irrelevant for this comparison. We find that the integrated background flux was brighter in November than in December by $2 \pm 0.5\%$, in good agreement with the expected change based on the increase in the path–length through the zodiacal plane between visits and empirical estimates

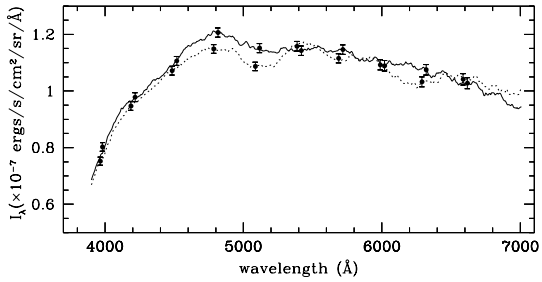

FIG. 16.— Surface brightness of the total background detected in the FOS spectra. The solid and dashed lines show the average of all six spectra taken during the November and December 1995 visits, respectively. The error bars indicate 1σ statistical errors of 1.5-2% per 300Å resolution element.

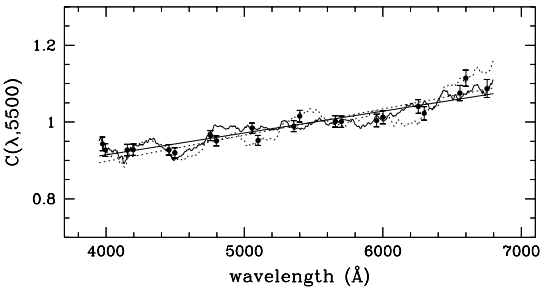

FIG. 17.— Color of the detected background with respect to solar. Solid and dashed lines show the detected background in the November and December 1995 data sets, respectively, divided by the Neckel & Labs (1984) solar spectrum at matched resolution. Straight lines show the linear fits. The error bars show the statistical error per resolution element in the FOS spectra. The adopted solar spectrum is simply the fiducial spectrum from which the ZL color is defined, and so it contributes no error here. For further discussion, see Paper II.

from ground-based observations (Levasseur–Regourd & Dumont 1980).

Employing the usual definition of the ZL color relative to the solar spectrum (see §2.2), we find $C(7000, 4000) = 1.044$ for the November visit, and 1.075 in the December data, as shown in Figure 17 with 1σ statistical uncertainty of 0.05%. The reddening of the ZL relative to the solar spectrum is a function of the scattering angle and, thus, also of time of year. Again, the trend we observe is in good agreement with the Helios Space Probe observations and others (see Leinert *et al.* 1981, and Leinert *et al.* 1998 for a review). We stress, however, that the FOS spectrum includes both the EBL and the ZL, and therefore we cannot measure the color of the ZL explicitly from these observations. It is only possible to determine the ZL color separately from the EBL by explicit measurement of ZL absorption features over a wide range in wavelength. All published colors of the ZL to date rely on broad–band observations. Separation of the ZL from other the EBL and DGL is discussed further in §11 and in detail in Paper II.

An error budget for the absolute flux calibration of these data is shown in Table 5 as the error per resolution element. The random error in the mean flux over the entire spectrum goes down as the square root of the number of resolution elements ($\sqrt{10}$). As discussed in §11, random and systematic errors have been combined assuming Gaussian and flat distributions, respectively. For comparison with the WFPC2 observations, we have integrated the FOS spectrum through the F555W bandpass (see Figure 5) and find the two results in good agreement. This comparison is subject to the systematic uncertainties in both data sets.

8. DIFFUSE GALACTIC LIGHT (DGL)

8.1. *Structured Component*

A diffuse, non–isotropic, optical background is produced in the Milky Way by scattering of the optical interstellar radiation field (ISRF) by Galactic dust. The same dust is heated by the UV ISRF, causing it to produce thermal IR emission. It is not surprising, therefore, that the thermal Galactic emission seen in the IRAS 100 μm maps correlates well with the surface brightness of the optical diffuse Galactic light (DGL), as both are proportional to the column density of the dust and the intensity of the ambient ISRF along the line of sight. In Tables 6 and 7, we give a representative summary of the observed correlations between optical and 100μm fluxes for regions with low to moderate 100 μm intensities (N(HI)$< 5\times10^{20}$ cm^{-2}, $I_{100} < 5$ MJy sr^{-1}) and a range of Galactic orientations.

As evident from those results, there is only moderate agreement concerning the exact scaling relations between the optical DGL and thermal emission at any wavelength. Measurement errors in the IR, optical, and UV intensities are $> 10\%$ in most cases and are one cause for variations between results. However, asymmetry in the scattering phase function of Galactic dust also contributes to the variable scaling relations seen between different lines of sight. Strong forward scattering causes lower optical surface brightnesses at both high latitudes ($|b| > 50°$) and at longitudes away from the Galactic Center ($130° < l < 230°$) (see Draine & Lee 1984, and references therein; Onaka & Kodaira 1991; Witt, Friedmann, & Sasseen 1997). Both trends are evident from the data shown in Tables 6 and 7.

While these results suggest a range of appropriate correlation factors, they do not identify a single appropriate scaling law for our purposes for two reasons. First, variability in the measured IR–optical and UV–optical correlations is evident within a single cloud, as well as between clouds (see, for example, Figures 5 & 6 in GT89 and Table 1 in Laureijs, Mattila, & Schnur 1987). This suggests that the observed systems may be dense enough that self-shielding and further complications come into play. These clouds have been selected precisely because the optical and IR emission is bright enough to be readily observed: while the IR flux levels and N(HI) column densities of the clouds listed in Tables 6 and 7 are low enough that the molecular gas fraction does not affect the correlation between dust column density (or extinction) and N(HI), they are still roughly a factor of 10 higher than the values for our observed field, for which $I_{100} \sim 0.4$ MJy sr^{-1}(N(HI) $\sim 0.47\times10^{20}$ cm^{-2}, or E($B-V$)$\sim$ 0.009 mag). Second, while empirical relations between the scattered and thermal DGL have have been published in the far–UV and at optical B– and R–bands, the expected surface brightness from scattering at 3000Å is not clear from these

TABLE 6
OBSERVED CORRELATIONS: $I_\lambda(0.16\mu\mathrm{m})/I_\nu(100\mu\mathrm{m})$

Reference	l° [a]	$\lvert b^\circ\rvert$[a]	$I_\lambda(0.16)/I_\nu(100)$[b]	$I_\lambda(0.16)/I_\nu(100)$[c]	$I_\nu(100)$[d]
Witt et al. (1997)[e]	$\langle 145\rangle$	$\langle 30\rangle$	72	0.86×10^{-9}	$2-8$
Hurwitz et al. (1991)[f]	$135-220$	>40	$80(\pm10)$	0.96×10^{-9}	$1-5$
Sasseen *et al.* (1996)	$\langle 270\rangle$	$\langle 45\rangle$	<233	$<2.8\times10^{-9}$	$2-8$
Jacobsen et al. (1987)	$\langle 70\rangle$	$\langle 50\rangle$	$65(\pm25)$	0.78×10^{-9}	$1-2$
Witt et al. (1997)	$\langle 290\rangle$	$\langle 45\rangle$	258	3.10×10^{-9}	$2-8$

[a]Bracketed values of Galactic longitude (l) and latitude (b) indicate average coordinates for the data used in the calculation.

[b]I_λ is in photons s^{-1} cm^{-2} $\mathrm{sr}^{-1}\text{Å}^{-1}$. I_ν is in units of $\mathrm{MJy\,sr}^{-1}$.

[c]I_λ is in ergs s^{-1} cm^{-2} sr^{-1} Å^{-1}.

[d]$I_\nu(100\mu\mathrm{m})$ is in $\mathrm{MJy\,sr}^{-1}$.

[e] Witt et al. (1997) use a model which is based on their observations and which includes the average scattering angle and phase function along the line of sight to predict $I_\lambda(0.16\mu\mathrm{m})/I_\nu(100\mu\mathrm{m})$ at the Galactic position indicated.

[f]We calculate $I_\lambda(0.16\mu\mathrm{m})/I_\nu(100\mu\mathrm{m})$ for Hurwitz et al. (1991) from the points plotted in their Figures 2a and 2b.

TABLE 7
OBSERVED CORRELATIONS: $I_\nu(\lambda)/I_\nu(100\mu\mathrm{m})$

Reference	$l(^\circ)$	$b(^\circ)$	$I_\nu(0.45)/I_\nu(100)$[a]	$I_\nu(0.65)/I_\nu(100)$[a]	$I_\nu(0.90)/I_\nu(100)$[a]	$I_\nu(100)$[a]
GT89 - ir1[b]	174	-42	0.36×10^{-3}	1.1×10^{-3}	...	11.4
Laureijs et al. (1987)[c]	211	-37	0.48×10^{-3}	...	...	6.3
GT89 - ir2[b]	235	37	1.1×10^{-3}	2.2×10^{-3}	$<1.6\times10^{-3}$	3.6
Paley et al. 1991	104	-32	4.8×10^{-3}	8.0×10^{-3}	11.0×10^{-3}	2.5
GT89 - ir3[b]	38	45	2.6×10^{-3}	4.4×10^{-3}	6.0×10^{-3}	5.9

[a]I_ν is in units of $\mathrm{MJy\,sr}^{-1}$, throughout. 1 $\mathrm{MJy\,sr}^{-1} = 10^{-17}c/\lambda^2$ ergs s^{-1} cm^{-2} sr^{-1} Å^{-1}.

[b]Guhathakurta & Tyson (1989) – field designation.

[c]From the data in Table 1 of Laureijs *et al.* (1987)

TABLE 8
MODEL CORRELATIONS: $I(\lambda)/I(100\mu\mathrm{m})$

$\lambda(\mu\mathrm{m})$	$\tau_\lambda/\mathrm{N(HI)}$[a]	ω_λ[b]	$S(g,b)$[c]	$I_\lambda(\lambda)/I_\nu(100)$[d]	$I_\nu(\lambda)/I_\nu(100)$[e]	$I_\lambda(\lambda)/I_\nu(100)$[f]
0.16	0.120	0.410	0.42	181.96	1.86×10^{-4}	2.18×10^{-9}
0.25	0.130	0.550	0.50	94.54	3.69×10^{-4}	1.77×10^{-9}
0.30	0.105	0.581	0.54	118.09	7.97×10^{-4}	2.66×10^{-9}
0.45	0.068	0.600	0.56	68.75	1.57×10^{-3}	2.32×10^{-9}
0.55	0.047	0.600	0.59	42.85	1.78×10^{-3}	1.77×10^{-9}
0.65	0.042	0.600	0.61	32.66	2.24×10^{-3}	1.59×10^{-9}
0.80	0.032	0.540	0.68	18.82	2.41×10^{-3}	1.13×10^{-9}
0.90	0.025	0.500	0.71	11.76	2.14×10^{-3}	7.94×10^{-10}

[a]Optical depth as a function of HI column density in units of $10^{20}\,\mathrm{cm}^{-2}$. Values are from Savage & Mathis (1979) and are in good agreement with the standard value of $\mathrm{A}_V/\mathrm{N(HI)}=0.06\,\mathrm{mag}/(10^{20}\,\mathrm{cm}^{-2})$ (Bohlin, Savage & Drake 1978).

[b]Albedo values from models of Draine & Lee (1984).

[c]Scattering phase function in terms of asymmetry parameter, g and Galactic latitude ($b = 50°$), as calculated by Draine & Lee (1984).

[d]$I_\lambda(\lambda)$ is in photons $\mathrm{s}^{-1}\mathrm{cm}^{-2}\mathrm{sr}^{-1}\text{Å}^{-1}$. $I_\nu(100\mu\mathrm{m})$ is in $\mathrm{MJy\,sr}^{-1}$.

[e]$I_\nu(\lambda)$ is in $\mathrm{MJy\,sr}^{-1}$. $I_\nu(100\mu\mathrm{m})$ is in $\mathrm{MJy\,sr}^{-1}$.

[f]$I_\lambda(\lambda)$ is in ergs s^{-1} cm^{-2} sr^{-1} Å^{-1}. $I_\nu(100\mu\mathrm{m})$ is in $\mathrm{MJy\,sr}^{-1}$.

results. Neither the optical depth of interstellar dust nor the ISRF is a monotonic function of wavelength between 1600Å and 4500Å (see Savage & Mathis 1979 and Mathis, Mezger, & Panagia 1983).

To better understand the contribution of non–isotropic DGL over the full range of our observations, we have used a basic scattering model to predict the scattered light from dust. We then compare the results of this model to the observed DGL at UV and optical wavelengths.

Assuming the Galactic cirrus along the line of sight in question is optically thin (extinction, $A_\lambda < 1.08\,\mathrm{mag}$), the surface brightness of scattered light off of interstellar dust can be expressed as

$$I_\lambda = j_\lambda\,\omega_\lambda\,\tau_\lambda\,[1 - 1.1g\sqrt{\sin b}], \qquad (4)$$

in which j_λ is the flux of the radiation field in ergs s^{-1} cm^{-2} sr^{-1} Å^{-1}; ω_λ is the effective albedo of the dust; τ_λ is the optical depth; and the term in brackets is the back–scattered intensity in terms of Galactic latitude, b, and the average phase function of the dust, g (Jura 1979). For strong forward scattering, $g \sim 1$; for isotropic scattering, $g \sim 0$. We take the ISRF flux, j_λ, from the Mathis et al. (1983) estimate for the Solar Neighborhood (10 kpc from the Galactic center). As our observations are $b = 60°$ from the Galactic plane and $l = 206\overset{\circ}{.}6$ from the Galactic center, this estimate is probably slightly high. We take the dust albedo from the results of Draine & Lee (1984), which are based on an exponential distribution in grain sizes suggested by Mathis, Rumpl & Nordsieck (1977).

The optical depth of Galactic dust, τ, is well known to correlate strongly with hydrogen column density (see Savage & Mathis 1979, Boulanger & Pérault 1988, and references therein). It is not surprising, then, that the thermal emission, I_{100}, also correlates well with hydrogen column density. While optical depth is a physical manifestation only of the column density of dust, I_{100} is also affected by the strength of the ISRF. We therefore use the observed I_{100} and $I_{100}/\mathrm{N(HI)}$ as calibrated by Boulanger & Pérault (1988) from the IRAS 100 μm maps to obtain an effective optical depth for our observations as follows. Optical depth can be written as a function of optical extinction and dust column density as

$$\tau_\lambda = 0.921\frac{R_\lambda}{N(\mathrm{H}i)/E(B-V)}\,N(\mathrm{H}i), \qquad (5)$$

in which $R_\lambda = A_\lambda/\mathrm{E}(B-V)$ is the usual expression for the normalized extinction. Several groups find $\mathrm{N(HI)}/\mathrm{E}(B-V)$ between 48×10^{20} and 50×10^{20} $\mathrm{cm}^{-2}\,\mathrm{mag}^{-1}$ from measurements of the HI densities from 21 cm line emission strength and the reddening to globular clusters and star counts (Bohlin, Savage & Drake 1978, Burstein & Heiles 1982, Knapp & Kerr 1974). To get an effective optical depth (weighted by the ISRF field strength which is at issue for scattering), we use the relation found by Boulanger *et al.* (1996) for the low–column density regime ($\mathrm{N(HI)} < 5\times10^{20}$ cm^{-2}): $I_{100}/\mathrm{N(HI)} \propto 0.85$ MJy $\mathrm{sr}^{-1}/(10^{20}\,\mathrm{cm}^{-2})$.[3] The fluxes in our field are roughly 0.4 MJy sr^{-1}, or $0.47\times10^{20}\,\mathrm{cm}^{-2}$. The predicted scattered fluxes from this model are shown in Table 8. Scattering angle is not considered in this model. Consequently, this estimate is conservative in the sense that it should overpredict the DGL for our observations, as the line of sight

[3]A slightly different scaling, $I_{100}/\mathrm{N(HI)} \propto 0.53$ MJy $\mathrm{sr}^{-1}/(10^{20}\,\mathrm{cm}^{-2})$, is seen in from the DIRBE results (Boulanger *et al.* 1996). The difference is attributed to a well known calibration offset in the IRAS maps. Since we are using IRAS fluxes, we use the IRAS correlation.

to our field is away from the Galactic center and the dust is forward scattering.

This scattering model reproduces the observed flux ratios with reasonable accuracy in the range 1600–4500Å (see Tables 7 and 6 at $b > 45$). The phase function changes by less than 10% at latitudes $|b| > 50°$, so the values shown in Table 8, for which $|b| = 50°$ was used, are generally representative for high latitude fields. However, as noted by GT89, optical colors $(B-R)$ and $(R-I)$ are redder than a basic scattering model predicts. GT89 find values of $I_\nu(R)/I_\nu(B) = 3.2$, 2, and 1.7 and $I_\nu(I)/I_\nu(R) = 2.3$, 2.1, and < 1.5 in three different fields. By comparison, the ratios we predicted are $I_\nu(R)/I_\nu(B)$=1.4 and $I_\nu(I)/I_\nu(R)$ = 0.95. A significant Hα contribution as the explanation for the red colors is ruled out by GT89. Variable scattering asymmetry with wavelength is another possible explanation, but strong wavelength dependence in the range 4500–9000Å has never been observed in the lab or in space (Witt *et al.* 1997, Onaka & Kodaira 1991, Laureijs *et al.* 1987). The most plausible explanation is suggested by observations of reflection nebulae, which have high N(HI) and show red fluorescence from molecular hydrogen, hydrogenated amorphous hydrocarbons, and polycyclic aromatic hydrocarbons. The relevance of such contributions to fields with 10 times lower N(HI) and I_{100}, as is the case for our data, is not clear, as the density of molecular gas correlates only with high column densities, N(HI) $> 5{\times}10^{20}\,\mathrm{cm}^{-2}$. The results of GT89, in fact, do show that the degree of reddening is well correlated to the average I_{100} emission but not structure within the cloud. Self–shielding, local optical depth and local ISRF may be responsible for strong variations in the correlation between color and molecular gas density both in and between fields (Stark 1992, 1995). It seems conservative, therefore, to adopt optical colors found for the fields with the lowest IR flux in the GT89 sample, listed in Table 7. Note that the IR flux in the 2 lower flux fields (denoted "ir2" and "ir3") is still more than a factor of 10 higher than in our own.

In summary, we estimate the optical flux in our field using our scattering model for $\lambda < 4500$Å, and adjust the predicted scattering model at redder wavelengths to match the average colors observed by GT89: $I_\nu(R)/I_\nu(B) \sim 1.8$ and $I_\nu(I)/I_\nu(R) \sim 2.0$. We apply this correction in the sense of increasing the long wavelength fluxes over that predicted by our models, so that the DGL estimate we use is, if anything, *higher* than is appropriate, although given the small total flux associated with the DGL even a large fractional decrease in our estimate of the DGL would have a negligible impact on our EBL results. The resulting spectrum is flat in I_λ, with a value of roughly 0.9–1.0$\times10^{-9}$ ergs s^{-1} cm^{-2} sr^{-1} Å^{-1} from 3000–9000Å. We note, also, that our scattering model was not dependent on Galactic longitude, which, again, makes ours a conservative overestimate of the DGL contribution to the total sky background, and our measurement of the EBL, therefore, a conservative underestimate in this regard.

8.2. *Isotropic Component*

Line emission and continuum processes from warm ionized gas in the Galaxy also contribute an isotropic component to the DGL. For $|b| > 5°$, Reynolds (1992) finds that Hα emission strength matches the prediction of a path–length through a slab model for the galaxy, $I(\mathrm{H}\alpha) \approx 2.9 \times 10^{-7} \csc|b|$ ergs s^{-1} cm^{-2} sr^{-1}. Fortunately, Hα emission, specifically, is irrelevant for us because the relative throughput of the F555W bandpasses at Hα ($\sim$ 6562Å) is only $\sim$10% of the peak filter throughput. The strongest Hα emission expected in our field would contribute 0.01$\times10^{-9}$ergs s^{-1} cm^{-2} sr^{-1} Å^{-1}, which corresponds to 0.01% of the total background, and 1% of the expected EBL. The next strongest line, [OIII] at 5007Å, is near the peak of the F555W sensitivity, but it is fainter than Hα by a factor of 20 (Reynolds 1985, Shields *et al.* 1981) and will contribute at most 0.05% of the expected EBL.

More important than line emission is the two–photon, free–free, and bound–free continua emitted by ionized gas with the density implied by the detected Hα emission. The combined spectrum of free–free, bound–free, and two–photon emission was calculated by Aller (1987) as a function of electron and ion densities, and has been expressed by Reynolds (1992) as a function of the observed Hα emission; it is a function of the temperature of the warm ionized medium. For our purposes, a conservative estimates of the isotropic continuum from gas with temperature $T \sim 10^4$ is given by Aller (1987) and Reynolds (1992) as $I_\lambda(\lesssim 3700\mathring{A}) < 0.3{\times}10^{-9}$ergs s^{-1} cm^{-2} sr^{-1} Å^{-1} and $I_\lambda(\gtrsim 3700\mathring{A})$ <0.01$\times10^{-9}$ergs s^{-1} cm^{-2} sr^{-1} Å^{-1} (see Aller 1987 and Reynolds 1992 for discussion). We include these contributions in our estimate of the DGL.

9. MEASUREMENT OF ZODIACAL LIGHT

To measure the ZL contribution to the background flux that we measured with HST, we obtained ground–based spectra at 3900-5100Å within the field of view of our WFPC2 images using the Boller & Chivens spectrograph on the duPont 2.5m Telescope at Las Campanas Observatory in Chile on the nights of 26–29 November 1995, concurrently with the HST observations of that field on 29 November 1995. We have used those spectra to measure the absolute flux of the ZL at 4650Å with a precision of 0.6%, and a systematic uncertainty of 1.0%, using the method outlined in §2. We also mesure the color of the zodiacal light to be $C(5100, 3900) = 1.05 \pm 0.01$. That measurement is discussed in detail in Paper II.

To identify the ZL flux contributing to the FOS and WFPC2 measurements of the total sky flux, we need an absolute, flux–calibrated spectrum of the ZL from roughly 2000–1μm (see WFPC2 bandpasses plotted in Figure 5). We obtain this spectrum by scaling a solar spectrum to the surface brightness value we measure for the ZL at 4650Å and applying a small reddening correction redward and blueward of 4650Å to compensate for the changing scattering efficiency of the interplanetary dust (see §2.2 for discussion). Although our LCO measurement of the ZL color is quite accurate, it only covers a small fraction of the total wavelength range covered by our WFPC2 observations. We therefore use our FOS observations to identify the appropriate reddening correction, which cover the wavelength range 4000–7000Å. Published measurements of the ZL color have absolute uncertainties as large as 10% and are in poor agreement with each other (see Leinert 1998). Our FOS observations, by contrast, are accurate to better than 2% in relative flux as a function of wavelength and are identical in line of sight and epoch to the

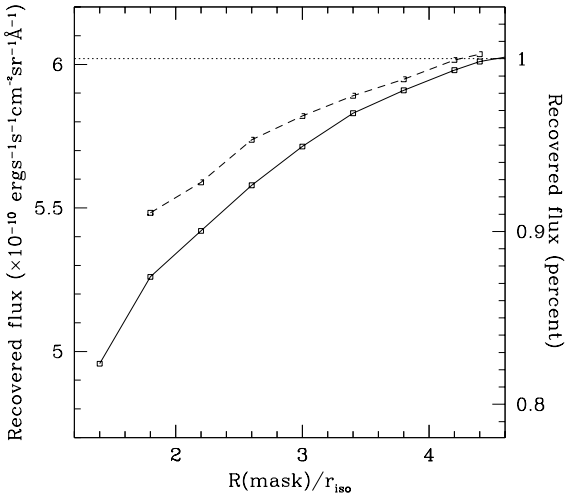

FIG. 18.— The ensemble flux recovered from apertures around detected galaxies ($V > 23$ AB mag) as a function of the radius of the apertures. Radius is given in terms of the limiting isophotal radius ($r_{\rm iso}$) for each galaxy. The solid line shows the flux recovered when $r_{\rm iso}$ is unconstrained; for the faintest objects, $r_{\rm iso}$ may be less than 3 pixels (the 90% encircled energy radius of WFPC2). The dotted line shows the flux recovered when a 3 pixel minimum is imposed for $r_{\rm iso}$. Note that the curve has not yet converged at the limit of the mask size plotted here.

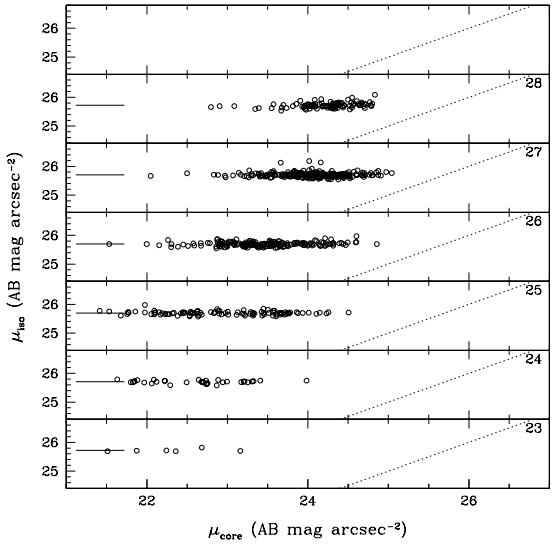

FIG. 19.— Isophotal surface brightness, $\mu_{\rm iso}$, versus core surface brightness (mean surface brightness in the brightest 4 pixels), $\mu_{\rm core}$, for all detected galaxies in the EBL images in unit magnitude bins $22 < V_{555} < 28$; the faintest bin with data shows $27 < V < 28$. In each plot, the diagonal lines (right) mark the limit $\mu_{\rm iso} = \mu_{\rm core}$; the horizontal lines (left) show the mean $\mu_{\rm iso}$, defined by sky noise ($1\sigma_{\rm sky}$). As expected, this does not change with magnitude. The distribution in $\mu_{\rm core}$ narrows at fainter apparent magnitudes, suggesting that surface brightness biases and detection limits may be causing incompleteness at the fainter magnitudes. The detection limit occurs at $V = 27.5$ AB mag, at which the average galaxy has $\mu_{\rm iso} - \mu_{\rm core} \sim 1.5$ mag arcsec^{-2}. The requirement for detection in our data is $\mu_{\rm core} < 2\sigma_{\rm sky}$ in the central 4 pixels.

WFPC2 and LCO observations. Like most measurements of the ZL, however, the FOS observations clearly include the EBL flux. This fact prevents the FOS and LCO results from unambiguously determining the color of the ZL. Fortunately, this is not an insurmountable problem: the WFPC2 observations can be used as a further constraint, as we describe in the following section.

10. EBL FROM RESOLVED SOURCES IN WFPC2 IMAGES

10.1. *Ensemble Photometry*

The total flux from resolved sources defines a lower limit to the EBL. Typically, such minima are obtained by measuring the flux in individual resolved sources using standard photometry packages, such as FOCAS (Valdes 1982, Jarvis & Tyson 1981) or SExtractor (Bertin & Arnouts 1996), and summing the flux in the resulting catalog of objects (c.f. Tyson *et al.* 1989, Madau *et al.* 1996, 1998). While it is quite straightforward to measure an isophotal magnitude, it is very difficult, if not impossible, to measure the total flux of an object including that flux in regions fainter than the noise level of the local sky. Efforts at measuring galaxy counts often attempt some sort of "total magnitude" correction, either by scaling the isophotal aperture to include roughly twice the isophotal extent (see Bertin et al. 1998 for discussion) or by applying a magnitude correction to galaxies near the detection limit (c.f. Smail *et al.* 1995).

Fortunately, individual source photometry is not necessary for estimating a lower limit to the EBL in our data. We have developed a simplified method of aperture photometry with which we can measure the flux from the ensemble galaxy population as a whole. We first use SExtractor to identify detectable sources and their isophotal radii ($r_{\rm iso}$) using detection and extraction parameters very similar to those employed in Williams *et al.* (1996) (see §4.4). We can then measure the "sky" surface brightness, $\mu_{\rm sky}$, for an image by masking all detected sources ($V_{555} \lesssim 27.5$ AB mag) and computing the average surface brightness of the remaining pixels. In doing so, we implicitly assume that extragalactic sources fainter than this limit contribute negligibly to the EBL, so that the apparent background level in the image consists only of foreground sources.[4] To estimate the total surface brightness from extragalactic sources and foregrounds, $\mu_{\rm obj+sky}$, we mask all stars and only galaxies brighter than $V_{\rm cut} = 23$AB mag and again compute the average surface brightness of the remaining pixels. We then isolate the flux from resolved sources, the minimum value of EBL23, by differencing the two surface brightness estimates: minEBL23 $\equiv \mu_{\rm obj} = \mu_{\rm obj+sky} - \mu_{\rm sky}$. In contrast to standard aperture photometry, $\mu_{\rm obj+sky}$ will always include all of the light from faint galaxies. However $\mu_{\rm sky}$ can include galaxy flux if the masks are too small.

Not surprisingly, minEBL23 from this method of ensemble photometry is a strong function of the mask size. The growth curve plotted in Figure 18 shows that at least 20% of the flux from galaxies within 4.5 magnitudes of the detection limit ($23 < V < 27.5$ AB mag) lies beyond $\sqrt{2} \times r_{\rm iso}$ for individual galaxies. As discussed in Williams

[4]We point this out not because we believe that the flux in galaxies beyond the detection limit is negligible, but rather as a reminder that the sum in detected galaxies is by definition a minimum value for the detected EBL.

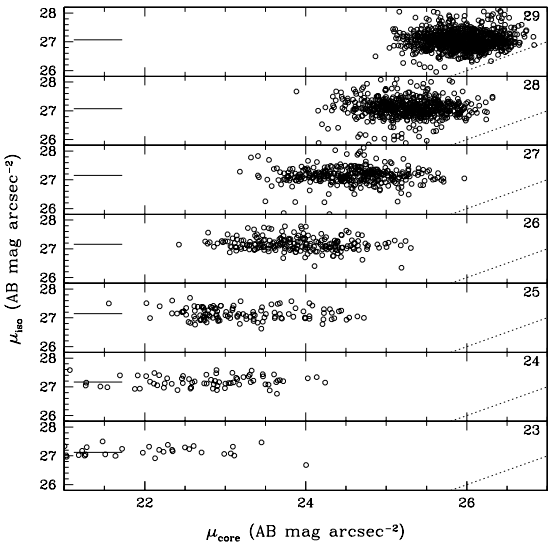

FIG. 20.— The same quantities as plotted in Figure 19 are shown for the galaxies in the HDF F606W catalog (Williams *et al.* 1996). The detection limit of the HDF catalog for V_{606} is quoted as 28.2 AB mag, which corresponds to a 10σ detection in the drizzled images ($\sim 2\sigma_{\rm sky}$ in 4 pixels in the original images). At $V_{606} = 28.2$AB mag, a typical galaxy has $(\mu_{\rm iso} - \mu_{\rm core}) \lesssim 1$ mag arcsec^{-2}. See Appendix B.2 for discussion.

et al. (1996), it is possible for the faintest galaxies detected to have isophotal radii which are smaller than the WFPC2 90% encircled energy radius for a point source (0.3 arcsec, or 3 pixels). To explore the effect of this resolution limit, we also show in Figure 18 the growth curve which results if we impose 0.3 arcsec as a minimum for $r_{\rm iso}$ and increase the mask size relative to that new starting radius. Naturally, the improvement in recovered flux is significant: in the HDF catalog of Williams *et al.* , nearly all galaxies with $V_{606} > 27.5$ ABmag are affected by this size requirement. While the instrumental PSF clearly contributes to the increasing recovered flux with radius, the growth curve is not entirely due to PSF effects: the 100% encircled energy radius would be reached by a mask of radius $2.5r_{\rm iso}$ if the smallest galaxies were physically contained within the original isophotal radii.

In addition to the fact that apertures extending to twice each galaxy's isophotal area will not recover all of the galaxy light from detected galaxies, the "local sky" estimates used in standard photometry packages come from regions just beyond the apertures for each source. These sky estimates will undoubtedly include a significant fraction of this missed light, doubly compounding the photometry errors.

While the growth curve in Figure 18 is beginning to level off by $4r_{\rm iso}$, it is clearly not flat. The covering factor of galaxies to $4r_{\rm iso}$ is roughly 20% in these images, and roughly 30% of the galaxies defined by these apertures overlap. In the HDF images, more than 1800 galaxies are found beyond our detection limit, with a covering factor of roughly 80% to $4r_{\rm iso}$. These facts suggest that we have reached a confusion limit of sorts, in the sense that the wings of detectable galaxies are overlapping. Moreover, these facts suggest that the wings of detectable galaxies contribute flux to a significant fraction of the pixels used to measure the foreground "sky" level, producing an extragalactic "pedestal" level which blends with the diffuse flux from ZL and DGL. Even though the flux level of our growth curve in Figure 18 is clearly converging, it cannot be used to quantify this pedestal of overlapping galaxy wings.

To estimate the flux contained in the wings of galaxies beyond $4r_{\rm iso}$ in our own images, we have constructed a Monte Carlo simulation of the contribution to a random point on the sky from randomly distributed, detectable galaxies. The surface number density of detectable galaxies was drawn from the published HDF catalog and exponential light profiles were adopted for all galaxies, with scale lengths and central surface brightness matching the galaxies in the EBL and HDF images. Efforts to characterize the light profiles of faint galaxies have produced evidence for both exponential disks and flatter, irregular profiles (for example, see Smail *et al.* 1995, Driver *et al.* 1995, Brinchmann *et al.* 1998, Driver *et al.* 1998 and references therein). For the faintest galaxies, profiles are unconstrained. We adopted exponential profiles here, in part because they produce the most conservative (smallest) estimate of the light beyond the $4r_{\rm iso}$ apertures. Also, given that the physical scales at those radii are large, we expect to be beyond any central bulges. We also note that the additional flux identified by our models from the faintest galaxies is less than 10% of the flux in galaxy counts by standard methods, and so is the adopted profiles for the faintest galaxies are not a critical issue to the minimum EBL estimates. The simulations are described in Appendix B. For the F555W EBL images, we estimate that the additional flux from galaxies beyond $4r_{\rm iso}$ is roughly 1.1×10^{-10} ergs s^{-1} cm^{-2} sr^{-1} Å^{-1}. The simulations are affected only by the surface brightness limits, galaxy profiles, and the galaxy surface densities adopted. Similar levels are therefore found for the F814W images, for which galaxy parameters and detection limits are very similar to those at F555W. The F555W aperture masks have been used to recover the flux from sources in all three bands for reasons discussed below. In the very low signal–to–noise ratio F300W images, only 20% of the F555W sources are detected, and the F555W aperture masks for those which are detected extend to many more than four times the F300W isophotal detection areas. Due to the larger statistical uncertainties in the flux recovered by ensemble photometry at F300W (see Table 10), simulations of the flux beyond the detection apertures were not warranted.

By using different values for $V_{\rm cut}$ (23, 24, 25 and 26 AB mag), we can isolate the flux contributed from galaxies in successive magnitude bins. Comparing these measurements with the integrated flux from standard photometry methods (see §4.4), we find that roughly 15%, 25%, 45% and 65% of the total flux in successive 1 magnitude bins between $23 < V_{555} < 27$ is contained at radii between $\sqrt{2}r_{\rm iso}$ and $4r_{\rm iso}$. In our data, galaxies with magnitudes $23 < V_{555} < 27.5$ have $1.5 < \Delta\mu < 3.5$ mag arcsec^{-2} as shown in Figure 19. These measurements are in broad agreement with the models in the literature for the fraction of flux which can be recovered as a function of $\Delta\mu$ based on extrapolation of simple exponential profiles (c.f. Disney & Phillipps 1983, Davis 1990, Dalcanton 1998).

The total flux in resolved galaxies as measured by en-

TABLE 9
SUMMARY OF MEASUREMENTS

Source	Bandpass	Data source	Flux	Random	Systematic
Total	F300W	HST/WFPC2	33.5	(± 4.9%)	[± 5.6%]
Background	F555W	HST/WFPC2	105.7	(± 0.3%)	[± 1.4%]
	F814W	HST/WFPC2	72.4	(± 0.2%)	[± 1.4%]
	F555W[a]	HST/FOS	111.5	(± 0.7%)	[± 2.8%]
Zodiacal	4600–4700Å	LCO	109.4	(± 0.6%)	[± 1.1%]
Light	F300W	LCO[b]	28.5	(± 0.6%)	[-1.1%,+1.2%]
	F555W	LCO[b]	102.2	(± 0.6%)	[-1.1%,+1.1%]
	F814W	LCO[b]	69.4	(± 0.6%)	[-1.3%,+1.1%]
Diffuse	F300W	DGL model	1.0	···	[+25%,-50%]
Galactic	F555W	DGL model	0.8	···	[+25%,-50%]
Light	F814W	DGL model	0.8	···	[+25%,-50%]

NOTE.—All fluxes are in units of 1×10^{-9}ergs s^{-1} cm^{-2} sr^{-1} Å^{-1}. For a source with constant flux in F_λ, filters F300W, F555W, and F814W have effective wavelengths $\lambda_0(\Delta\lambda)$ =3000(700), 5500(1200), and 8100(1500)Å. For a source with a solar spectrum, effective wavelengths are λ_0 = 3200, 5500, 8000Å.

[a]Observed FOS spectrum, convolved with the WFPC2/F555W bandpass to allow direct comparison with the WFPC2 results.

[b]LCO measurement of zodiacal light, extrapolated to the WFPC2 bandpass by applying a correction for changing zodiacal light color with wavelength relative to the solar spectrum. The zodiacal light flux through the WFPC2 bandpasses was identified using SYNPHOT models, the uncertainty due to which is included in the uncertainty for the filter calibration and is shared with the systematic uncertainty for the total background flux.

TABLE 10
EBL RESULTS AND UNCERTAINTIES

Bandpass	Random σ_R (68%)	Systematic σ_S (68%)	Combined σ (68%)	EBL($\pm1\sigma$)
Detected EBL23 (WFPC2 + LCO)[a]				
F300W	2.1	1.5	2.5	4.0 (±2.5)
F555W	0.6	1.3	1.4	2.7 (±1.4)
F814W	0.4	0.9	0.0	2.2 (±1.0)
Minimum EBL (WFPC2)[a]				
F300W	0.19	0.13	0.22	3.2 (±0.22)
F555W	0.003	0.009	0.01	0.89 (±0.01)
F814W	0.002	0.007	0.01	0.76 (±0.01)
Detected EBL23 (FOS + LCO)[a]				
F555W	0.7	2.7	2.8	8.5 (±5.6)
Flux from detected sources in HDF ($m > 23$ AB mag)				
F300W				0.66
F450W				0.51
F606W				0.40
F814W				0.27
Published number counts[b]				
F300W ($18 < U_{300} < 23$ AB mag)				0.27 (±0.05)
F555W ($15 < V_{555} < 23$ AB mag)				0.49 (±0.10)
F814W ($13 < I_{814} < 23$ AB mag)				0.65 (±0.13)

NOTE.—All fluxes and errors are given in units of 10^{-9} ergs s^{-1} cm^{-2} sr^{-1} Å^{-1}.

[a]The systematic and statistical errors have been combined assuming a flat or Gaussian probability distribution, respectively, as discussed in §11. We equate 1σ combined errors with the 68% confidence interval, as the combined errors are nearly Gaussian distributed. Individual sources of error contributing to these totals are summarized in Tables 3 and 4 of this paper and in Table 1 of Paper II.

[b]Estimated errors correspond to uncertainties in the fits to published galaxy counts. The values given correspond to 0.081×10^{-20}, 0.46×10^{-20}, and 1.5×10^{-20} in units of ergs s^{-1} cm^{-2} sr^{-1} Hz^{-1} and are consistent with those used in Pozzetti et al. (1998).

semble photometry has two obvious implications for galaxy counts. First, the total flux in galaxy counts based on standard photometry will significantly underestimate the EBL. This point is discussed further in the following sections. Second, because standard photometry will miss fractionally more light from the faintest galaxies, the galaxy counts which result will have an artificially shallow slope at the faint end. Our results allow us to derive "aperture corrections" for faint galaxy photometry as a function of central and isophotal surface brightness. This is done in Paper III. We can use these corrections to recalculate the surface number density of galaxies as a function of magnitude. As we discuss in detail in Paper III, the corrected number counts do not flatten out at the faintest limits of the HDF.

10.2. *Discussion: Minimum EBL23*

Using the ensemble photometry method described above, we measure the flux from detectable sources relative to the mean sky level in the F300W, F555W, and F814W images of our own data to be 3.19×10^{-9}, 6.02×10^{-10}, and 5.16×10^{-10}, respectively.[5] For the F300W and F814W images, we use the masks derived from the F555W images in order to guarantee that the same sources are contributing to the minimum EBL23 at all wavelengths. The 1800 galaxies detected in the HDF with V_{606} magnitudes in the range 27.5–30 AB mag (see Figure 4.4) are clearly not included in our estimate of the minimum EBL23 derived by ensemble photometry.

The contribution from galaxies in the HDF catalog with $V_{555} > 27.5$ AB mag is 0.57×10^{-10}ergs s^{-1} cm^{-2} sr^{-1} Å^{-1} at V_{555} as measured by standard photometric methods. In keeping with the discussion in the previous section, we estimate that only 35% of the light is recovered from galaxies with $27.7 < V_{606} < 30$ AB mag in the HDF, so that the true flux from these sources is roughly 1.8×10^{-10}ergs s^{-1} cm^{-2} sr^{-1} Å^{-1}. Adding this to the flux from detected sources ($23 < V_{555} < 27.5$) in our EBL field, we find the total flux from detected sources ($23 < V_{555} < 30$) to $4r_{\rm iso}$ apertures to be 7.8×10^{-10}ergs s^{-1} cm^{-2} sr^{-1} Å^{-1}. Adding to this the estimated extragalactic contribution to the background sky level beyond $4r_{\rm iso}$ (Figure B.1), we identify the minimum flux from detected galaxies with $V_{555} > 23$ AB mag to be 8.9×10^{-10}ergs s^{-1} cm^{-2} sr^{-1} Å^{-1}. We emphasize that this estimate of the minimum EBL23 is indeed a minimum estimate from which sources will be excluded due to the surface brightness biases and detection limits of our own images as well as the HDF (see Figures 19 and 20). Incompleteness due to surface brightness detection limits is discussed further in Paper III.

Following the same method for F300W and F814W data leads to the minimum EBL23 values summarized in Table 10. The total combined statistical and systematic error for this minimum EBL23 measurement is roughly $\pm1\times10^{-11}$ ergs s^{-1} cm^{-2} sr^{-1} Å^{-1}, $\times100$ smaller than the error for the EBL23 detections because the conversion to physical units can occur after foregrounds are subtracted. Comparing the total flux from detected galaxies measured using ensemble photometry versus standard methods, the photometry errors affecting standard methods are clearly worse at UV wavelengths where signal–to–noise ratio is lower, calibration is less accurate, and the instrumental PSF is broader than in the other filters.

[5]For comparison, the flux measured by standard photometry for sources with AB magnitudes between 23 and 27.5 in the HDF are 6.7, 5.1, 3.8, and 2.5×10^{-10}ergs s^{-1} cm^{-2} sr^{-1} Å^{-1} in the F300W, F450W, F606W, and F814W, respectively.

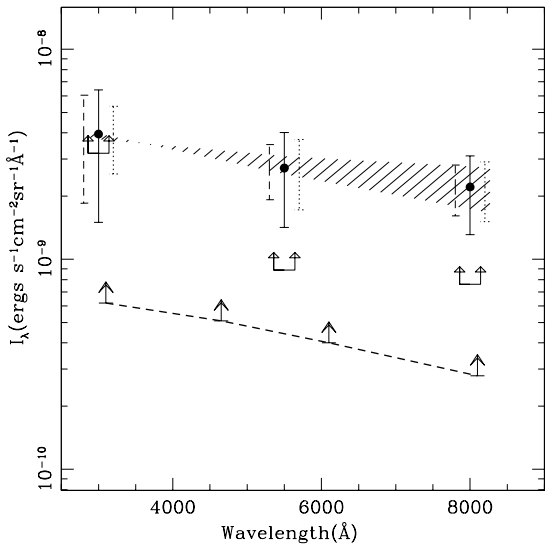

FIG. 21.— Filled circles show the EBL23 obtained using the HST/WFPC2 EBL images, the ZL flux measured at (4650Å), and the nominal ZL color as described in §11. The solid error bars (centered on the filled circles) show the combined 1σ errors while the dotted (offset by +100 Å) and long–dashed (offset by -100 Å) error bars show 1σ systematic and random errors, respectively. The hatch–marked region shows the 1σ uncertainty in the detected EBL due to uncertainty in ZL color. The lower limit arrows connected by a dashed line indicates the total flux from individually photometered galaxies with magnitudes $23 < V_{555} < 30$ AB mag in the HDF catalog. The u-shaped lower limit arrows show minEBL23, the flux from detectable galaxies in the EBL fields with $23 < V_{555} \leq 28$ AB mag as determined by ensemble photometry as described in §10.

11. EBL DETECTIONS

The detected EBL in each of the three WFPC2 bands is the difference between the total sky flux in the WFPC2 images, $I_{\rm Total}$, and the foreground flux from ZL and DGL. As described in §8.1, the DGL contribution has no spectral features, is relatively flat in I_λ, and is easily subtracted. The spectrum of the zodiacal light is uniquely defined by our measurement of the mean flux of the ZL at 4650Å, the solar spectrum, and the color of the ZL as follows:

$$I_{\rm ZL}(\lambda) = I_\odot(\lambda)\, C(\lambda, 4650)\, \frac{I_{\rm ZL}(4650)}{I_\odot(4650)}. \qquad (6)$$

(See the Appendix A for a discussion of the solar reference spectrum, $I_\odot$, used and the convolution of $I_{\rm ZL}(\lambda)$ with the WFPC2 bandpasses to obtain the ZL flux through each filter.)

Both the mean flux and color of the zodiacal light in the range 3900–5100Å are uniquely determined by our LCO data. However, the color over the wavelength range of the WFPC2 data is less certain. From our LCO data, we find $C(5100, 3900) = 1.05 \pm 0.01$ from absolute surface spectrophotometry of the ZL. As discussed in §7, we find $C(7000, 4000) = 1.044 \pm 0.01$ from our FOS spectra. Although this is in excellent agreement with the LCO results, extragalactic contributions are included in the FOS

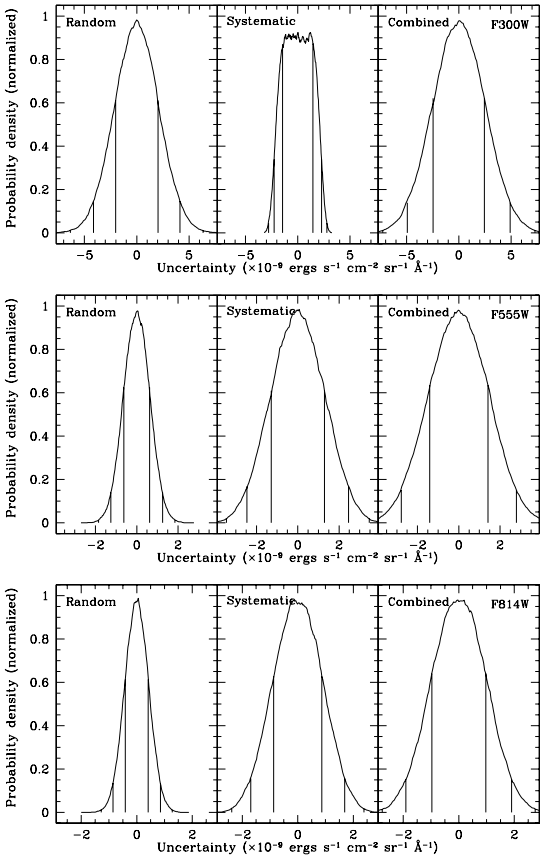

FIG. 22.— Combined probability distributions of the errors (systematic, random, and combined) for the EBL flux detected in the F300W (panel a), F555W (panel b), and F814W (panel c) WFPC2 bandpasses. A flat (Gaussian) probability distribution was assumed for each contributing systematic (random) error. The vertical lines show 68.3%, 95.4%, and 99.7% confidence intervals, which we use to define 1, 2 and 3σ values for the combined errors.

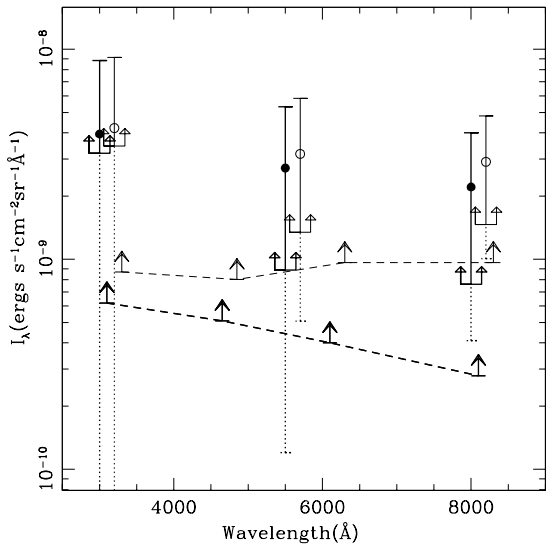

FIG. 23.— The detected background light from galaxies fainter than $V_{555} = 23$ AB mag is marked by large filled circles with 2σ error bars. The error bars are dotted where they extend below the flux recovered from galaxies in the range $23 < V_{555} < 28$ AB mag by the aperture photometry method (see §10) shown by the u-shaped lower limit symbols. The integrated flux from galaxies in the HDF, from 23 AB mag to the detection limit at each wavelength (29–30 AB mag), is marked by lower limit arrows connected by the thick, dashed line. The total flux in galaxy counts, HDF counts plus ground–based counts brighter than $V_{555} = 23$ AB mag is shown by lower limit arrows connected by a thin dashed line. The open circles (displaced by 200Å for display purposes) show the EBL we detect, plus the integrated ground–based counts brighter than $V_{555} = 23$ AB mag. We have not included uncertainties in the ground-based counts in the error bars shown.

spectrum. We have therefore devised a method to further constrain the ZL color using the WFPC2 results.

Between 2000Å and 1μm, the color of the zodiacal light relative to the solar spectrum as a function of wavelength is empirically known to be roughly linear with wavelength; the mean flux with respect to the Sun becomes redder by roughly 5%/1000Å over the range from 2500Å–1.4μm. No deviations from a linear color are apparent in our FOS spectra, which are the first observations to have the required broad–band calibration sensitivity to address this question. To constrain the ZL and EBL surface brightness in all three bands, we therefore begin by assuming that the color of the ZL is a linear function of the solar spectrum with wavelength and that any small deviations from linearity average out over the 1000Å bandwidths of the WFPC2 filters.

Only if the EBL is flat in I_λ would the color of the EBL plus ZL be the appropriate color to adopt for the ZL. If, for example, the EBL is blue in I_λ, then the ZL is slightly redder. At 3000, 5500, and 8000Å, we have already identified minima for the EBL. If we adopt these minima for the EBL at 3000 and 8000Å, we can obviously infer that the maximum possible flux for the ZL is what remains when we subtract the DGL and the minimum EBL from the total surface brightness detected in each band. By considering the maximum possible $I_{\rm ZL}$ at 3000 and 8000Å, and comparing those maxima to the absolute flux which we have measured at 4650Å, we constrain the color of the ZL to be $3.0\%/1000\text{Å} < C(\lambda, \lambda_o) < 5.0\%/1000\text{Å}$. This estimate is in excellent agreement with the color we find for the total background as measured by FOS, which was 4.4%/1000Å redder than solar. Using these extrema for the color of the ZL, we can constrain the EBL at all three WFPC2 wavelengths (see Figure 21). We adopt this range as the 3σ uncertainty in the ZL color.

We calculate final statistical and systematic uncertainties from the WFPC2 and LCO measurements assuming a Gaussian probability distribution for each source of random error listed in Tables 3 and 4 and in Table 1 of Paper II. The final systematic uncertainties are calculated assuming a flat probability distribution for the systematic uncertainties listed in the same tables. Cumulative random and systematic errors are quoted and plotted separately to give a sense of the measurement limitations. In general, random errors reflect limitations in instrument sensitivity and stability, while systematic errors are dominated by stability of the flux calibration of each instrument and the accuracy of the flux calibration for the instruments relative to each other. Uncertainty in the DGL subtraction is not explicitly included in these combined errors, as the total DGL flux is relatively small and the error would not

contribute significantly to the total error. The DGL estimate was intended to be conservatively large, so that the EBL is, if anything, underestimated due to errors in the DGL.

We have also calculated combined errors (systematic and statistical) to obtain a final confidence interval. For this we have again assuming a Gaussian probability distribution for all of the random sources of error and a flat probability distribution for the systematic uncertainties. The combined error probability distributions are shown in Figure 22. In general, non-Gaussian systematic errors and Gaussian random errors cannot meaningfully be combined in quadrature. Nonetheless, given the large number (16) of individual sources of uncertainty contributing to our final errors, the combined uncertainty has a nearly Gaussian distribution, as expected. We therefore equate the 1σ combined errors for each bandpass with the 68% confidence intervals for the mean EBL23 detections and the lower limits, minEBL23. The final errors are summarized in see Table 10.

12. SUMMARY

We summarize our detection of the surface brightness of EBL23 from resolved and unresolved galaxies fainter than $V_{555} = 23$ AB mag as follows (in ergs s^{-1} cm^{-2} sr^{-1} Å^{-1}):

I_λ(F300W)$= 4.0\ (\pm 2.5)\ \times 10^{-9}$
I_λ(F555W)$= 2.7\ (\pm 1.4)\ \times 10^{-9}$
I_λ(F814W)$= 2.2\ (\pm 1.0)\ \times 10^{-9}$.

The quoted errors are 1σ combined uncertainties (statistical and systematic) corresonding to 68% confidence intervals, as described in §11. We can also define strict lower limits to the EBL from detected galaxies fainter than $V_{555} = 23$ AB mag by computing the flux from all detected objects using the "aperture photometry" method described in §10. The lower limits for EBL23 are (in ergs s^{-1} cm^{-2} sr^{-1} Å^{-1}):

$I_{23<V<27.5}$(F300W) $\geq 3.2\ (\pm 0.22)\ \times 10^{-9}$
$I_{23<V<27.5}$(F555W) $\geq 0.89\ (\pm 0.01)\ \times 10^{-9}$
$I_{23<V<27.5}$(F814W) $\geq 0.76\ (\pm 0.01)\ \times 10^{-9}$.

For comparison with predictions of the EBL based on the local metal mass density and total star formation history of the universe, the flux from galaxies brighter than $V_{555} = 23$ AB mag should be added to these results, as shown in Figure 23. We discuss these comparisons in Paper III.

It is a pleasure to thank A. Fruchter, R. Lyons, C. Keyes, A. Koratkar, L. Petro and D. Van Orsow for help in planning and scheduling the HST observations, and J. Christensen, H. Ferguson, and J. Keyes for help in understanding and improving the standard pipeline reduction for both the WFPC2 and FOS data. S. Baggett, S. Cassertano , R. Bohlin, and E. Smith also provided help with the WFPC2 and FOS calibration. We have also benefited greatly from discussions with J. Dalcanton, S. Shectman, T. Small, I. Smail, J. Trauger, and B. Weiner. R. Kurucz kindly provided an electronic version of the Solar Atlas. Finally, we would like to thank Carnegie Observatories and specifically L. Searle, A. Oemler, and I. Thompson for generous allocation of observing time at Las Campanas Observatory; the referee, R. Windhorst, for helpful comments; R. Blandford, A. Readhead, and W. Sargent for financial support to RAB during the first year of this work; and especially R. Williams for his support of this project. This work was supported by NASA through grants NAG LTSA 5-3254 and GO-05968.01-94A to WLF.

APPENDIX

MEAN ZODIACAL LIGHT FLUX THROUGH HST FILTERS

The fiducial solar spectrum we have used for the purposes of creating a low–resolution spectrum of the zodiacal light from 2500Å–1μm is a composite of the UV solar spectrum of Woods *et al.* (1997), the optical spectrum from NL84, and the infrared spectrum produced by Arvesen *et al.* (1969), as recommended by Colina, Bohlin & Castelli (1996). The accuracy of the absolute flux of this solar spectrum is irrelevant to the accuracy of the zodiacal light spectrum, $I_{\rm ZL}(\lambda)$; the absolute flux of $I_{\rm ZL}(\lambda)$ is defined by the measured flux of the ZL in our own LCO spectra at 4650Å, and by a combination of that measurement plus the color term, $C(\lambda, 4650\mathring{A})$, at all other wavelengths. The color term itself is simply an empirical description of color of whatever fiducial solar spectrum we adopted relative to the observed color of the zodiacal light as measured in our FOS data. Thus, the absolute flux of $I_{\rm ZL}(\lambda)$ is defined by the accuracy of the broad–band flux calibration of the FOS and LCO spectra, and the accuracy of the ZL measurement in the LCO spectra, as described in Paper II. The accuracy of the ZL measurement is, or course, dependent on the Solar Flux Atlas as discussed in Paper II.

The spectrum $I_{\rm ZL}(\lambda)$ as expressed in equation 6 is then an absolute flux-calibrated spectrum of the ZL, which we can convolve with the SYNPHOT throughput tables (using the version released in May 1997) in the usual way to obtain the absolute flux of the ZL through each of the filters. The flux through the WFPC2 band is given by

$$I_{\rm WF}(\lambda) = \frac{\int T(\lambda)\ I_\lambda(\lambda)\ \lambda\ d\lambda}{\int T(\lambda)\ \lambda\ d\lambda}, \qquad \text{(A1)}$$

in which $T(\lambda)$ is the effective throughput of a WFPC2 filter (including telescope and detector efficiencies), $I_\lambda(\lambda)$ is the spectrum of the zodiacal light, and all spectra are in units of ergs s^{-1} cm^{-2} sr^{-1} Å^{-1}. No additional error results from convolving the flux calibrated ZL with the bandpasses that define the WFPC2 system, as any error in the SYNPHOT synthetic photometry is incorporated in our estimate of the WFPC2 systematic uncertainty. See Paper II for a discussion of the LCO measurement of $I_{ZL}(4650\mathring{A})$.

FLUX FROM THE LOW SURFACE BRIGHTNESS WINGS OF DETECTED GALAXIES

In order to estimate the contribution from the wings of detected galaxies to the mean sky flux beyond $4r_{\rm iso}$ in a particular image, we have constructed a Monte Carlo simulation. In this simulation, we sum the cumulative flux contributed by randomly placed, detectable galaxies to a given point on the sky, such that the total galaxy popula-

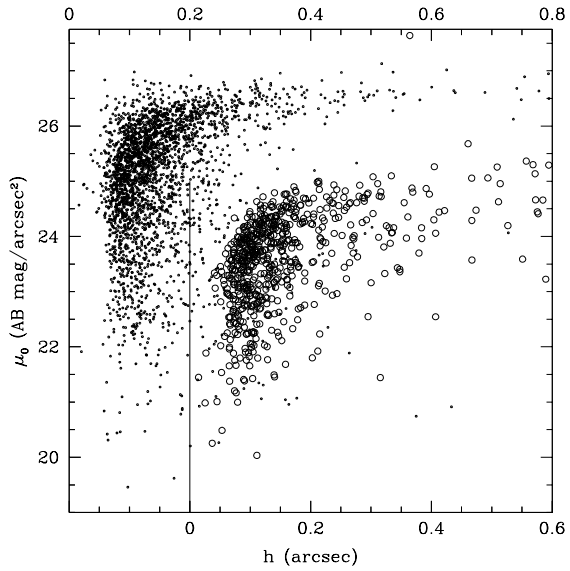

FIG. B1.— Fitted values of scale length, h, and central surface brightness, μ_0, for galaxies from the Figures 19 (EBL data, open circles) and 20 (HDF data, points) assuming exponential light profiles. The HDF galaxies are plotted relative to the X-axis at the top of the plot; EBL galaxies are relative to the lower X-axis for clarity. The feature in both data sets which trails off to high h at constant μ_0 corresponds to galaxies at the detection limit for which $\mu_{\rm iso} - \mu_0 \lesssim 1$.

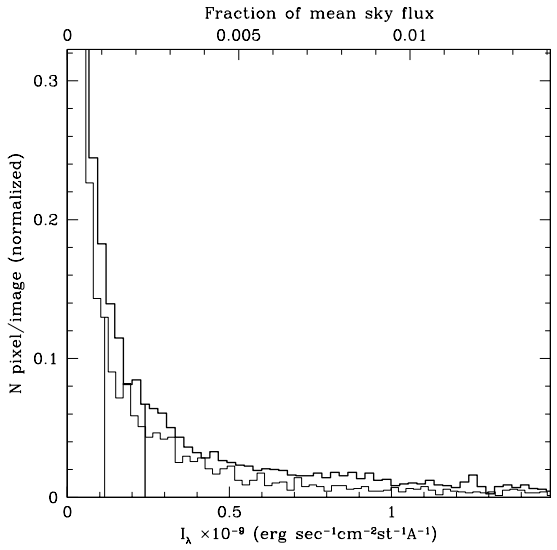

FIG. B2.— Histogram of flux per "sky pixel" found in two Monte Carlo simulations described in §10. Each trial models the flux contributed to a random point on the sky by nearby galaxies. The lower X-axis shows flux in cgs units, while the top X-axis shows the flux as a fraction of the the mean foreground sky flux (dominated by ZL) at the levels observed in the EBL WFPC2 field. Surface brightness limits and sky noise levels used in this simulation to define the detection region around the simulated sources reflect the parameters of the V_{555} EBL images. The thick line shows the sky pixel histogram which results from extending the "detection" aperture around simulated source to the $1.4r_{\rm iso}$. The thin line shows the histogram associated with detection apertures extending to $4r_{\rm iso}$. Vertical lines mark the mean "sky" flux identified in each simulation.

tion simulated reproduces the appropriate surface number density as a function of magnitude. If a randomly placed galaxy is close enough to the "sky pixel" that the pixel would fall within the detection aperture of the galaxy, then the trial is rejected and another begins. The extent of the galaxy apertures (how close galaxies can be to the sky pixel in question before that pixel falls within the galaxy's detection aperture) are determined based on the mean "foreground" sky level and noise characteristics assumed for the image being simulated. The simulation continues until we obtain 10,000 "sky pixels."

As faint galaxies are weakly clustered on small projected scales (Colley *et al.* 1996, 1997; Roche *et al.* 1993), we have simply placed galaxies randomly in this simulation. For the surface density of galaxies as a function of apparent magnitude, we have adopted the HDF galaxy counts at $V > 23$AB mag, which go 1.5 mag fainter than our own data (see Figure 4.4). We have assumed that the observed light profiles of faint galaxies are adequately described by an exponential profile, $\mu_r = \mu_0 \exp(-r/h)$, where μ_0 is the central surface brightness and h is the scale length. Using the measured values of the core surface brightness in the central 4 (undrizzled) pixels, $\mu_{\rm core}$, the isophotal surface brightness, $\mu_{\rm iso}$, and the isophotal radius, $r_{\rm iso}$ for the HDF galaxies, we can determine μ_0 and h (see Figures 19 and 20). As can be seen in Figures B.1 and B.2, h and μ_0 as a function of magnitude are consistent for our data and the HDF images, given the relative surface brightness limits of each.

EBL images

In Figure B.1, we plot histograms of the absolute flux contributed to 10,000 sky pixels at ≈ 5500Å in two simulations corresponding to the surface brightness limits of our F555W EBL images, $\mu_{\rm iso} = 1\sigma_{\rm sky} = 25.6 V_{555}$ AB mag arcsec^{-2}. In the first simulation, we define the regions associated with galaxies by the standard aperture size used for "total" magnitudes, $\sqrt{2}r_{\rm iso}$. In the second simulation, we extend the galaxy apertures to $4r_{\rm iso}$. In the first simulation, we find that the flux from wings of galaxies contributes 2.3×10^{-10}ergs s^{-1} cm^{-2} sr^{-1} Å^{-1} to the mean "sky" flux. As more galaxy light is excluded from the sky mean in the second simulation, the mean level of simulated "sky" pixels drops by just over 50% to 1.1×10^{-10}ergs s^{-1} cm^{-2} sr^{-1} Å^{-1}. The difference in flux in the "sky"pixels is within 10% of the flux we measured in the region $1.4-4r_{\rm iso}$ by ensemble aperture photometry, giving us confidence in our estimate of the flux coming from beyond $4r_{\rm iso}$. Note that the total flux from beyond the standard galaxy photometry apertures, 2.3×10^{-10} ergs s^{-1} cm^{-2} sr^{-1} Å^{-1}, is roughly $< 0.5\%$ of the mean sky level from diffuse zodiacal and galactic foregrounds, as indicated on the top x-axis of Figure B.1. Note further that while the extragalactic pedestal from galaxies outside of the $4r_{\rm iso}$ detection apertures is only 0.1% of the ZL plus DGL foreground flux and 5% of the detected EBL in §11, it is 20% of the *recovered* flux from galaxies with $V > 23$ AB mag by standard methods of galaxy photometry.

Comparison with the detection limits of the HDF

As discussed in §10, the crucial parameter for predicting the flux which will be recovered from a detected galaxy is the difference between the sky (limiting isophotal) sur-

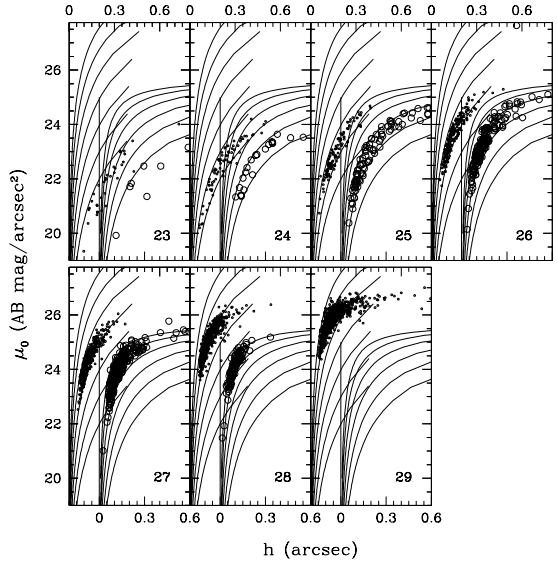

FIG. B3.— Each panel shows fitted h and μ_0 for galaxies in the HDF and EBL fields in unit magnitude bins. Axes and symbol types are as in Figure B.1. Lines show the μ_0 and h limits for galaxies with $m = 23, 24, ...29$. Galaxies in each magnitude bin can be seen to lie within the μ_0, h relation for that magnitude range with the exception of galaxies near the surface brightness limits of the data, for which profile solutions become ill-defined.

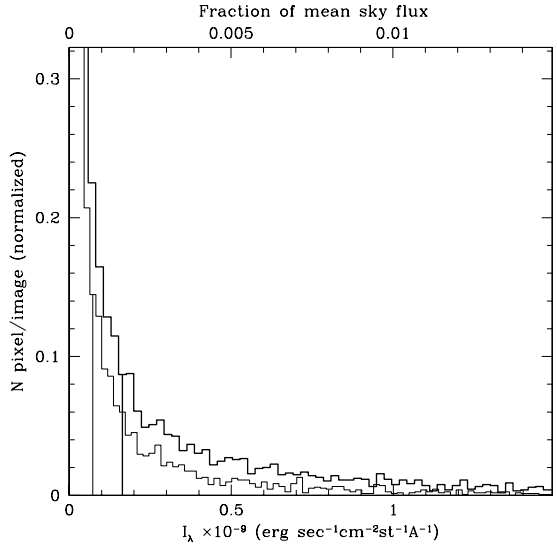

FIG. B4.— Same as Figure B.1, but for surface bright detection limits, noise characteristics, and mean sky flux of the HDF V_{606} images.

face brightness and the galaxy's core surface brightness, $\Delta\mu = \mu_{\rm sky} - \mu_{\rm core}$. The surface brightness detection limits of our data and HDF data are demonstrated in the Figures 19 and 20. Figure 20 demonstrates that galaxies in the HDF with $V_{606} = 29$ AB mag have $\Delta\mu \lesssim 1.0$mag arcsec^{-2} on average, with some galaxies in that bin nearly reaching the limit $\mu_{\rm sky} \approx \mu_{\rm core}$. If these galaxies have exponential profiles, then only $\sim 20\%$ of their total flux can be recovered by standard photometry methods. By analogy with our data, galaxy apertures which extend to $\sqrt{2}r_{\rm iso}$ in the HDF will miss at least 20% of the flux from galaxies in the range $25 < V_{606} < 29.5$ AB mag. This light will be included in the estimate of the local sky and thus subtracted from the flux within the galaxy aperture, doubling the total error.

We have run the same Monte Carlo simulations described in §B1 using parameters that describe the noise and sky statistics of the HDF. Using $\mu_{\rm iso} = 1\sigma_{\rm sky} = 27.1 V_{606}$ AB mag arcsec^{-2}, we find an extragalactic contribution to the mean sky flux of 1.6×10^{-10} and 0.8×10^{-10}ergs s^{-1} cm^{-2} sr^{-1} Å^{-1} for galaxy apertures extending to $1.4r_{\rm iso}$ and $4r_{\rm iso}$, respectively, as shown by the histograms in Figure B.2. As for our EBL images, this is in good agreement with estimates of the fractional flux that should be recovered from galaxies as a function of magnitude for the corresponding values of $\Delta\mu$. In order to calculate the total flux from galaxies detected in the HDF, we can sum the flux in the individual sources within standard, $1.4r_{\rm iso}$ apertures, and add to the resulting surface brightness *twice* the flux which lies outside of those apertures as identified from the simulated sky histogram for HDF detection parameters. Doing so, we find that the total corrected flux from detected galaxies in the HDF $23 < V_{606} < 31$ is 7.5×10^{-10}ergs s^{-1} cm^{-2} sr^{-1} Å^{-1} at 5850Å. Converting to the central wavelength of the V_{555} filter, this is roughly 9.1×10^{-10}ergs s^{-1} cm^{-2} sr^{-1} Å^{-1} at 5250Å, in good agreement with the total flux from sources in our EBL field, estimated in §10.2.

REFERENCES

Aller, L.H. 1987, in Physics of Thermal Gaseous Nebulae (Physical Processes in Gaseous Nebulae), (Dordercht: Reidel), Vol. 112, p.101
Arvesen, J.C., Griffin, Jr., R.N. & Douglas Persson, Jr., B. 1969, Appl. Opt., 8, 2215
IRAS Explanatory Supplement. 1986, ed. C.A. Beichman, G. Neugebauer, H.J. Habing, P.E. Clegg, & T.J. Chester (Washington: GPO)
Bernstein, R.A., 1998, Ph.D. Thesis, California Inst. of Tech.
Bernstein, R.A., Freedman, W.L. & Madore, B.F. 2001b, ApJ, submitted (Paper II)
Bernstein, R.A., Freedman, W.L. & Madore, B.F. 2001c, ApJ, submitted (Paper III)
Berriman, G.B., Boggess, N.W., Hauser, M.G., Kelsall, T., Lisse, C.M., Moseley, S.H., Reach, W.T. & Silverberg, R.F. 1994, ApJ, L63
Bertin, E. & Arnouts, S. 1996, AAS, 117, 393
Bohlin, R.C., Savage, B.D. & Drake, J.F. 1978, ApJ, 224, 132
Bohlin, R.C. 1995, in Calibrating HST: Post Servicing Mission, eds. A. Koratkar & C. Leitherer (Baltimore: STScI), 49
Boulanger, F. & Pérault, M. 1988, ApJ, 330, 964
Boulanger, F., Abergel, A., Bernard, J.–P., Burton, W.B., Désert, F.—X., Hartmann, D., Lagache, G. & Puget, J.–L. 1996, AA, 312, 256
Broadfoot, A.L. & Kendall, K.R., 1968, J. Geophys. Res., 73, 426
Burrows, C.J. 1991, in The First Year of HST Observations, eds. A.L. Kinney & J.C. Blades (Baltimore: STScI), 96
Burstein, D. & Heiles, C. 1982, AA, 87, 1165
Chamberlain, J. W., 1961, Physics of the Aurora and Airglow, (New York: Academic Press).
Colina, L. & Bohlin, R.C. 1994, AJ, 108, 1931
Colina, L., Bohlin, R.C. & Castelli, F. 1996, AJ, 112, 307
Dalcanton, J.J. 1998, ApJ, 495, 251
Disney, M. & Phillipps, S. 1983, MNRAS,205, 1253
Davies, J.I. 1990, MNRAS, 244, 8
Draine, B.T. & Lee, H.M. 1984, ApJ, 285, 89 (DL84)
Dube, R.R., Wickes, W.C. & Wilkinson, D.T. 1977, ApJ, 215, L51
Dube, R.R., Wickes, W.C. & Wilkinson, D.T. 1979, ApJ, 232, 333
Fabian, A.C. & Iwasawa, K. 1999, MNRAS, 303, L34
Guhathakurta, P. & Tyson, J.A. 1989, ApJ, 346, 773 (GT89)

Hamuy, M., Walker, A.R., Suntzeff, N.B., Gigoux, P., Heathcote, S.R. & Phillips, M.M. 1992, PASP, 104, 553
Hasan, H. & Burrows, C.J. 1993, in Calibrating Hubble Space Telescope, eds. J.C. Blades & S.J. Osmer (Baltimore: STScI), 395
Hayes, D.S. 1985, in IAU Symposium No. 111, Calibration of Fundamental Quantities, eds. D.S. Hayes, L.E. Pasinetti, & A.G. Davis Phillip (Reidel, Dordrecht), 225
Holtzman, J., Burrows, C.J. & Casertano, S. et al. 1995a, PASP, 107, 1065 (H95b)
Holtzman, J., Hester, J.J. & Casertano, S. et al. 1995b, PASP, 107, 156 (H95a)
Hurwitz, M., Bowyer, S. & Martin, C. 1991, ApJ, 372, 167
Infante, L. 1997, AAS, 107, 413.
Jacobsen, P., de Vries, J.S. & Paresce, F. 1987, AA, 183, 335
Jarvis, J.F. & Tyson, J.A. 1981, AJ, 86, 476
Jura, M. 1979, ApJ, 227, 798
Keyes, A., 1995, in Calibrating HST: Post Servicing Mission, eds. A. Koratkar & C. Leitherer, (Baltimore:STScI), 41
Knapp, G.R. & Kerr, F.J. 1974, AA, 35, 271
Kron, R.G. 1980, ApJS, 43, 305
Laureijs, R.J., Mattila, K. & Schnur, G. 1987, AA, 184, 269
Leinert, Ch., Richter, I., Pitz, E. & Planck B. 1981, AA, 103, 177
Leinert, Ch., et al. 1998, AAS, 127, 1
Levasseur–Regourd, A.C. & Dumont, R. 1980, AA, 84, 277
Lyons, R.W., Baity, W.A., Cohen, R.D. & Junkkarinen, V.T. 1993, in HST Calibration Workshop, eds. J.C. Blades & S.J. Osmer, (Baltimore:STScI), 229
Mathis, J.S., Mezger, P.G. & Panagia, N. 1983, AA, 128, 212
Mathis, J.S., Rumpl, W. & Nordsieck, K.H. 1977, ApJ, 217, 425
Mattila, K. 1976, AA, 47, 77
Mattila, K. 1990, in IAU Symposium 139, Galactic and Extragalactic Background Radation, ed. S. Bowyer & Ch. Leinert (Dordrecht: Kluwer), 159
Murthy, J., Henry, R.C., Feldman, P.D. & Tennyson, P.D. 1990, AA, 231, 187
Matsuura, S., Matsumoto, T. & Matsuhara, H. 1995, Icarus 115, 199
Neckel, H. & Labs, D. 1984, Sol. Phys., 90, 205
Onaka, T. & Kodaira, K. 1991, ApJ, 379, 532
Paley, E.S., Low, F.J., McGraw, J.T., Cutri, R.M. & Rix, H.-W. 1991, ApJ, 376, 335
Pozzetti, L., Madau, P., Zamorani, G., Ferguson, H.C. & Bruzual A.G. 1998, MNRAS, 298, 1133
Qi, J., Barnes, A.V., Espy, S.L., Riehl–Chudoba, M., Sun, C.–N., Albridge, R.G. & Tolk, N.H. 1991, Appl. Phys. Let., 59, 16
Reynolds, R.J. 1985, ApJ, 298, L27
Reynolds, R.J. 1992, ApJ, 392, L35
Roche, N., Shankes, T., Metcalf, N., & Fong, R. 1993, MNRAS 263, 360
Röser, S. & Staude, J. 1978, AA, 67, 381
Sasseen, T.P. & Deharveng, J.–M. ApJ, 1996, 469, 691
Savage, B.D. & Mathis, J.S. 1979, ARAA, 17, 73
Shields, G.A. et al. 1981, ApJ, 248, 569
Smail, I., Hogg, D.W., Yan, L. & Cohen, J.G. 1995, ApJ, 449, L105
Stark, R. et al. 1992, AJpS, 79, 77
Stark, R. 1995, AA, 301, 873
Toller, G.N. 1983, ApJ, 266, L79
Valdes, F. 1982, Faint Object Classification and Analysis System, KPNO Internal Publication
Whitmore, B., Heyer, I. & Casertano, S. 1999, PASP, 111, 1159
Williams, R.E. et al. 1996, AJ, 112, 1335
Witt, A.N., Friedmann, B.C. & Sasseen, T.P 1997, ApJ 481, 809
Woods, T.N. et al. 1996, J. Geophys. Res. 101, D6